The Egyptian Journal of Remote Sensing and Space Sciences 27 (2024) 577–596

Contents lists available at ScienceDirect

The Egyptian Journal of Remote Sensing and Space Sciences

journal homepage: www.sciencedirect.com

Research Paper

PRISMA vs. Landsat 9 in lithological mapping – a K-fold Cross-Validation implementation with Random Forest

Ali Shebl [a,b], Dávid Abriha [c,*], Maher Dawoud [d], Mosaad Ali Hussein Ali [e], Árpád Csámer [a,f]

[a] Department of Mineralogy and Geology, Faculty of Science and Technology, University of Debrecen, Egyetem tér 1, 4032 Debrecen, Hungary
[b] Department of Geology, Tanta University, 31527 Tanta, Egypt
[c] Department of Physical Geography and Geoinformatics, Faculty of Science and Technology, University of Debrecen, Egyetem tér 1, 4032 Debrecen, Hungary
[d] Department of Geology, Faculty of Science, Menoufia University, Egypt
[e] Mining and Metallurgical Engineering Department, Assiut University, Assiut 71515, Egypt
[f] Cosmochemistry and Cosmic Methods Research Group, University of Debrecen, Debrecen 4032, Hungary

ARTICLE INFO

Keywords:
PRISMA
Landsat 9
Random forest
Geological mapping

ABSTRACT

The selection of an optimal dataset is crucial for successful remote sensing analysis. The PRISMA hyperspectral sensor (with 240 spectral bands) and Landsat OLI-2 (boasting high dynamic resolution) offer robust data for various remote sensing applications, anticipating their increased demand in the coming years. However, despite their potential, we have not identified a rigorous evaluation of both datasets in geological applications utilizing Machine Learning Algorithms. Consequently, we conduct a comprehensive analysis using Random Forest, a widely-recommended machine learning algorithm, and employ K-fold cross-validation (with $K = 2, 5, 10$) with grid-search hyperparameter tuning for enhanced performance. Toward this aim, diverse image-processing approaches, including Principal Component Analysis (PCA), Minimum Noise Fraction (MNF), and Independent Component Analysis (ICA), were applied to enhance feature selection and extraction. Subsequently, to ensure better performance of the RF algorithm, this study utilized well-distributed points instead of polygons to represent each target, thereby mitigating the effects of spatial autocorrelation. Our results reveal dataset-hyperparameter dependencies, with PRISMA mainly influenced by *max_depth* and Landsat 9 by *max_features*. Employing grid-search optimally balances dataset characteristics and data splitting (folds), generating accurate lithological maps across all K values. Notably, a significant hyperparameter shift at $K = 10$ produces the best lithological maps. Fieldwork and petrographic investigations validate the lithological maps, indicating PRISMA's slight superiority over Landsat OLI-2. Despite this, given the dataset nature and band count difference, we still advocate Landsat 9 as a potent multispectral input for future applications due to its superior radiometric resolution.

1. Introduction

Among several geological applications of remote sensing data, lithological mapping is still one of the most critical topics and several advancements have been introduced in this area (Shebl et al., 2024) especially with the availability of Machine Learning Algorithms (MLAs) (Shebl et al., 2023b). Accurate lithological mapping is a key solution for common complicated issues in mineral explorations (Shebl et al. 2021), landslide susceptibility (Chen et al., 2019), land use land cover analysis (Sun et al., 2022), groundwater potentiality mapping (Shebl et al., 2022), engineering geology (Chacón et al., 2006; Dearman and Fookes, 1974), and various geospatial suitability analyses (Prasad et al., 2014). Thus ensuring a solid base for a certain terrain by accurate identification of its lithological components could further save money, time, effort, and even souls. Significant advancements have been observed in this domain, evolving from traditional geological mapping methods involving on-leg mapping, progressing through the use of grey-scale aerial photography, and colored remote sensing combinations, ultimately leading to the adoption of Machine Learning Algorithms (MLAs) (Bahrami et al., 2024; Chen et al., 2024; Wang et al., 2024). However the latter introduced an objectivity that is always missed in conventional methods, model evaluation issues and selecting of the optimum parameters still the main challenges for most of MLAs(Al-Ruzouq et al., 2024; Bhat et al., 2024; Roy et al., 2024).

* Corresponding author.
E-mail address: abriha.david@science.unideb.hu (D. Abriha).

https://doi.org/10.1016/j.ejrs.2024.07.003
Received 21 December 2023; Received in revised form 4 June 2024; Accepted 9 July 2024
Available online 15 July 2024

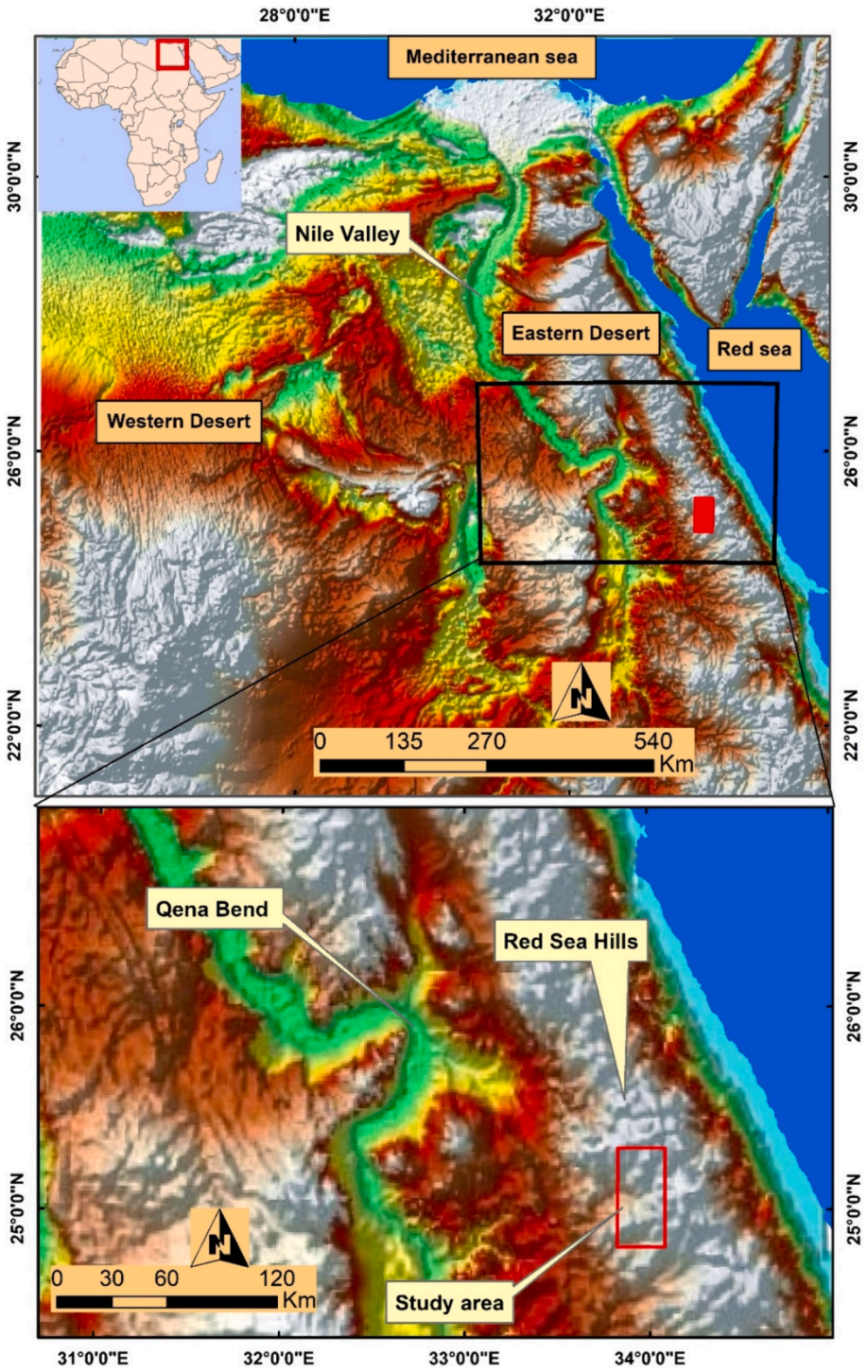

Fig. 1. Location map of the study area (red rectangle).

The widely used method of train-test splitting is simple and often gives good results with less computing power, but does not introduce a robust evaluation of the utilized model. This issue could be clearly manifested if the model performance is more sensitive to a particular, which could ultimately lead to biased classification in some cases. As a solution to the model evaluation issues, the K-fold cross-validation (KCV) method has been introduced and has achieved reliable generalizations in various applications (Anguita et al., 2012; Chang et al., 2024; Gholinejad et al., 2019; Phinzi et al., 2021; Yadav and Shukla, 2016). One of the main conundrums of KCV is selecting the *K* value as it affects trade-off between bias and variance. However, several researchers opt for *K* values such as 5 or 10 (striking reasonable balance between bias and variance) based on empirical evidence (Burman, 1989; Jung, 2018; Marcot and Hanea, 2021). Another issue that is almost always encountered in machine learning applications is the hyperparameter tuning (i.e. arguments). Trial and error remains a favored approach to hyperparameter optimization, with grid-search emerging as a powerful method that systematically explores all possible combinations of hyperparameter values during model training (Alibrahim and Ludwig, 2021; Yaloveha et al., 2022).

In addition to employing an effective method for hyperparameters optimization and robust machine learning model, the selection of a

Table 1
Characteristics of Landsat 9 and PRISMA.

Operational Land Imager 2 (OLI-2)			
Band	Spectral region	wavelength (μm)	Spatial resolution (m)
B1	Visible Coastal Aerosol	0.43–0.45	30
B2	Visible Blue	0.450–0.51	30
B3	Visible Green	0.53–0.59	30
B4	Red	0.64–0.67	30
B5	Near-Infrared	0.85–0.88	30
B6	SWIR 1	1.57–1.65	30
B7	SWIR 2	2.11–2.29	30
B8	Panchromatic	0.50–0.68	15
B9	Cirrus	1.36–1.38	30
Thermal Infrared Sensor 2 (TIRS-2)			
B10	TIRS 1	10.6–11.19	100
B11	TIRS 2	11.5–12.51	100
PRISMA			
Number of Bands		240	
Wavelength		400–2500 nm	
VNIR		66 channels within the range of 400–1100 nm	
SWIR		174 channels within the range of 920–2500 nm	
Spatial resolution		30 m for the hyperspectral bands 5 m for the panchromatic (PAN)	
Swath Width		30 Km	
Inclination		97.751°	
Orbital altitude		614.8 km	
Spectral width		≤ 14 nm	
Radiometric quantization		12 bits	
Spectral calibration accuracy		± 0.1 nm	
Signal-noise ratios		> 160, > 100, and > 240 for VNIR, SWIR, and PAN respectively	

Table 2
Characteristics of training and testing data points.

Class Name	Abbreviation	No. Data points
Serpentinite	SP	69
Talc-carbonates	TC	29
Basic metavolcanics with pillowed basalts	BB	31
Syn-orogenic granite and artisanal mining	SG	37
Metagabbro-diorite rocks	MGD	29
Acidic to intermediate Metavolcanics and tuffs	MVs	65
Volcaniclastic metasediments	VMs	65
Wadi deposits	WDs	60

powerful dataset is critical for achieving successful results. In remote sensing applications, ensuring better spectral discrimination is mainly attributed to an enhanced radiometric resolution for the utilized sensor. This could be simply illustrated by the definition of the radiometric resolution as the total number of distinct signals of a given strength that the sensor can capture (Pradham et al., 2008). Thus, a higher dynamic range could be more efficiently applied for many applications as it allows for greater information to be perceptible in the captured image. This aspect of sensor technology has been a focal point in satellite design, continuously advancing over time to ensure dependable and refined spectral discrimination. For instance, Landsat 7 sensor captures images with 8-bit resolution, enabling the measurement of 256 distinct grey values representing reflected energy. Ikonos-2 possesses an 11-bit radiometric resolution, allowing for the measurement of 2048 grey values (Pradham et al., 2008). Landsat-8 and Sentinel-2 sensors have 12-bit providing better spectral analysis compared to the lower dynamic ranges. Recently, Landsat-9 with its operational Land Imager 2 (OLI-2) provided increased details being discernible through its 14-bit resolution making Landsat-9 among the best optical sensors for several applications (Niroumand-Jadidi et al., 2022). Similarly, imaging spectroscopy with hundreds of bands is proven to be much more useful than multispectral data analysis for comprehensive spectral interpretations in geological applications.

Our ongoing research is primarily focused on evaluating both OLI2 and PRISMA datasets in lithological mapping using the Random Forest machine learning algorithm. To ensure robust classification and unbiased evaluation, our research incorporates grid-search hyperparameter tuning method and a k-fold evaluation technique, emphasizing the reproducibility of our findings for the scientific community.

2. Study area and geological setting

The basement rocks in Egypt form the northernmost section of the Nubian Shield, primarily located in the Red Sea hills (Fig. 1). This region is part of the larger Arabian Nubian Shield (ANS), which is considered an extension of the Mozambique belt and serves as a notable example of accretionary orogens and suturing (Abdelsalam and Stern, 1996; Stern, 1994). Situated within the Arabian Nubian Shield (ANS) and the far southern region of the Central Eastern Desert (CED), Um Salatit-Abu Meriewa district comprises ophiolitic rocks intricately combined with volcanic and sedimentary rocks from an island arc assembly (Shebl and Csámer, 2021; Zoheir et al., 2019). Moreover, there are intrusions of granitoid and gabbroid rocks, which have intersected the existing formations and, in certain zones, have effaced the primary geological structures (Khedr et al., 2023).

3. Materials and methods

3.1. Landsat 9

Launched in 2021, Landsat 9 employs Operational Land Imager 2 (OLI-2) to monitor Earth's changes. OLI-2 captures images in the visible, near-infrared, and shortwave-infrared spectrum at a pixel size of 30 m, with an added high-resolution panchromatic band (Band 8) at 15 m, as detailed in Table 1. Landsat 9 also features two thermal infrared (TIR) bands at a spatial resolution of 100 m, obtained using the TIR-2 sensor. Distinguishing it from Landsat 8 (OLI), Landsat 9 boasts a 4 TB solid-state recorder, a significant improvement over the 400 GB capacity of Landsat 8, utilized for onboard data storage (Wulder et al., 2022). Moreover, Landsat 9 exhibits enhanced brightness levels (radiometric resolution) with a 14-bit dynamic range, surpassing its predecessor OLI on Landsat 8, which had a 12-bit dynamic range. In the present investigation, a Landsat 9 scene (LC09_L2SP_174043_20220331_20220405_02_T1) devoid of clouds and exhibiting surface reflectance was employed to analyze the lithological attributes within the study area.

3.2. PRISMA

The Italian Space Agency launched PRISMA in March 2019 as a sun-synchronous hyperspectral sensor, offering 250 spectral channels spanning a wavelength range of 0.4–2.5 μm (Loizzo et al., 2019; Shebl et al., 2023a). PRISMA is a push broom sensor that has an internal calibration unit for better spectral data. Band designations and the spatial and spectral characteristics of PRISMA are shown in Table 1. Given its highly informative attributes (Table 1), PRISMA is anticipated to yield superior outcomes across various scientific domains. Recent research highlights the efficacy of PRISMA data in diverse fields such as environmental analysis and several geospatial applications (Aneece and Thenkabail, 2022; Bedini and Chen, 2022; Kokhanovsky et al., 2022; Giardino et al., 2020; Macusi et al., 2022). In this study, a PRISMA scene (PRS_L2C_STD_20210406082847_20210406082851_0001) with cloud-free surface reflectance was employed to examine the lithological features of the research area.

Both datasets are of second-level processing (L2), ensuring consistency in the preprocessing steps. Furthermore and using a GIS environment, we aligned the images geometrically to ensure that each pixel in one dataset corresponds spatially to the pixel in the other dataset. This step was crucial for maintaining spatial accuracy and ensuring the integrity of subsequent analyses.

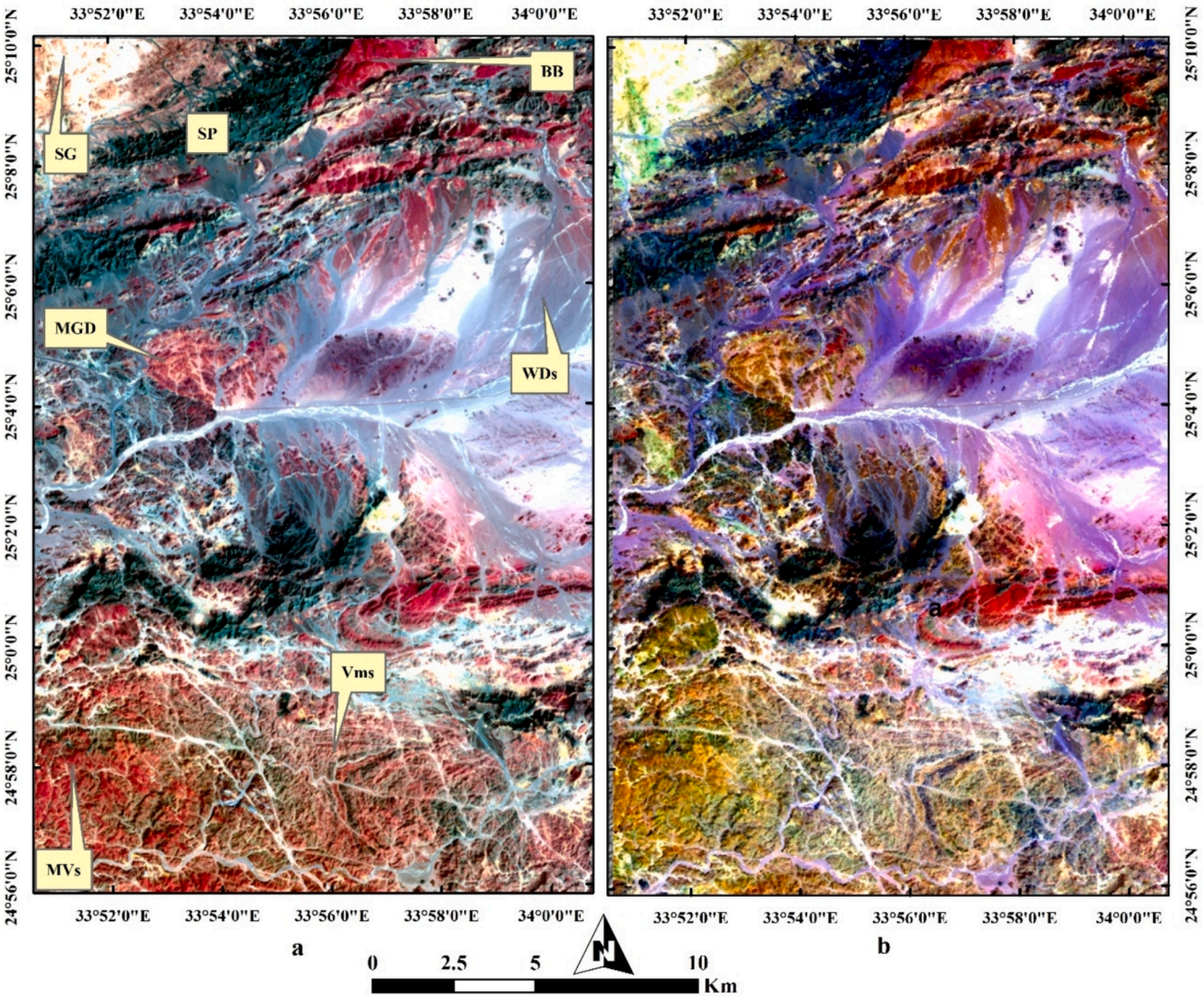

Fig. 2. Lithological discrimination illustrated through False Color Combinations: (a) Utilizing RGB channels with Landsat 9 bands 7–4-2, and (b) Employing the PRISMA satellite's SWIR bands 133–8 and VNIRband 17 in RGB, respectively.

3.3. Features selection and extraction

Spatial dependence between training and test data may result in overfitting that goes unnoticed when using cross-validation procedures for model selection and evaluation. When evaluating the effectiveness of machine learning models, spatial autocorrelation in spatial data presents difficulties. Due to the assumption of independent and identically distributed data, ignoring spatial autocorrelation can be unduly optimistic (Abriha et al., 2023; Meyer et al., 2018; Pohjankukka et al., 2017). A number of techniques, including dividing data into non-overlapping subsets like blocks or buffers, have been proposed (Le Rest et al., 2014; Pohjankukka et al., 2017) in order to address this problem. This study adopted well-distributed points (instead of polygons) representing each target to reduce the spatial autocorrelation effect.

Eight lithological targets (Table 2) were clearly delineated based on several image processing techniques, fieldwork and previous studies. False Color Composites (FCCs) generated from Landsat 9 (7/4/2 in RGB) and PRISMA (133/8/17 in RGB) effectively differentiate serpentinite rocks, portraying them in a profound black hue in contrast to the deep red tones of metavolcanics (Fig. 2). This distinction is clearly observed in Landsat 9 b7-b6-b2 RGB and PRISMA SWIR b139-SWIR b110-VNIR b13 representations, as depicted (Fig. 3). The chosen spectral bands for the FCCs predominantly fall within a comparable spectral range, highlighting similarities between (a) and (b) in Figs. 2 and 3. Additionally, all the other rock units could be reasonably identified (annotated in Fig. 2a). These spectral combinations proves instrumental in enhancing lithological mapping utilizing the two adopted sensors, particularly in analogous terrains.

To enhance lithological mapping and augment the reliability of training and testing datasets for the Random Forest (RF) algorithm, a comprehensive approach was employed. Principal Component Analysis (PCA), Minimum Noise Fraction (MNF), and Independent Component Analysis (ICA) were seamlessly integrated and applied across all bands of each sensor. The Landsat 9 Principal Components (PCs) (3/2/1 in RGB) depict serpentinites in a robust yellow hue, a characterization corroborated by the orange tones observed in PCs 1/3/2 in RGB for PRISMA. This distinct identification facilitates clear delineation, as illustrated in Fig. 4. Furthermore, meta gabbroic rocks exhibit a discernible yellowish tint in both PRISMA and Landsat 9 MNF combinations, as showcased in Fig. 5.

Fig. 6 depicts a reasonable discrimination of weathered *syn*-tectonic granites at the northwestern corner of the study area. Additionally, the contrast between metavolcanics and serpentinites is consistently evident

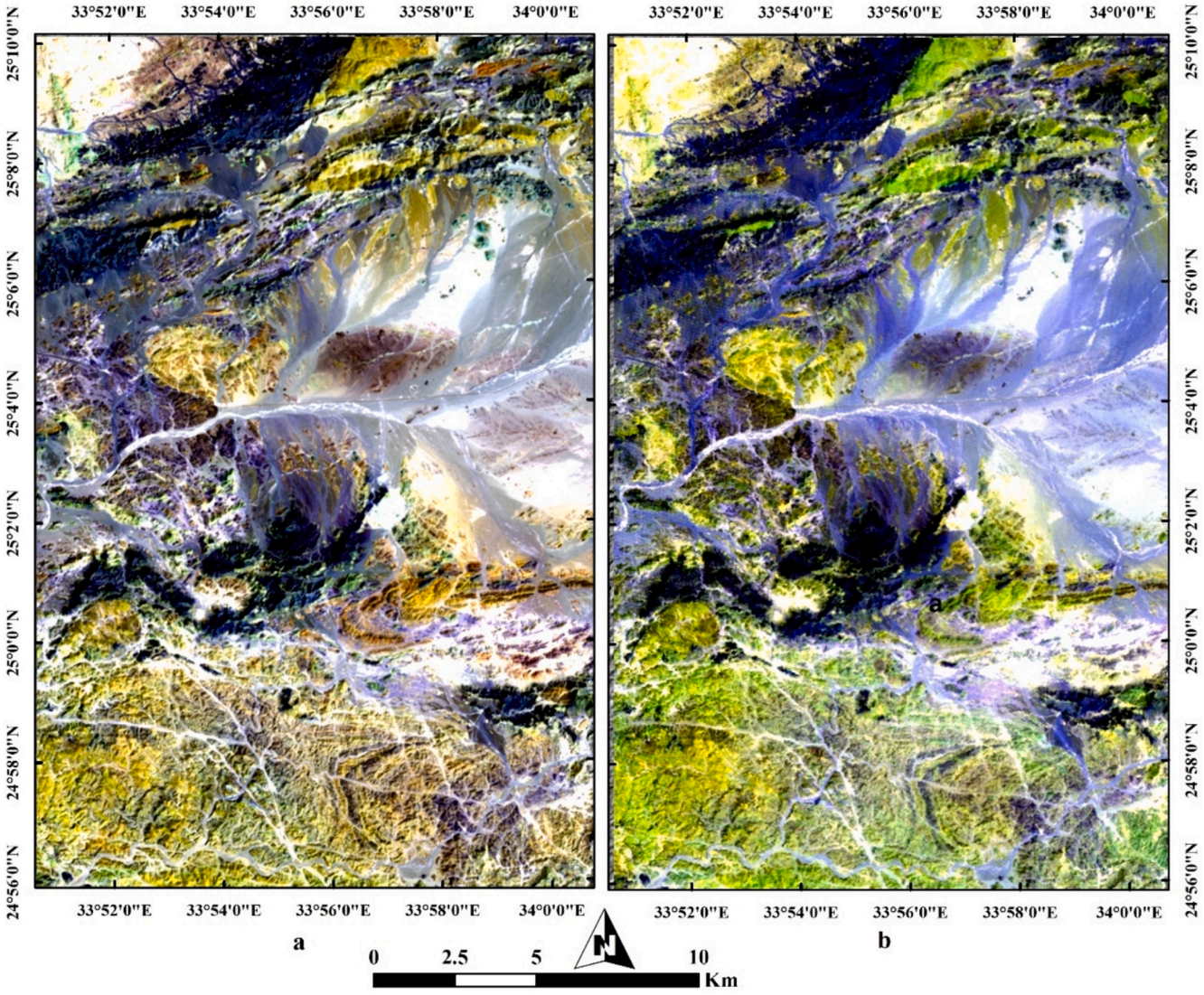

Fig. 3. Lithological discrimination illustrated through False Color Combinations: (a) Utilizing RGB channels with Landsat 9 bands 7–6-2, and (b) Employing the PRISMA satellite's SWIR bands 139–110 and VNIR band 13 in RGB, respectively.

across all image-processing findings. Independent Component Analysis (ICA) introduced a distinctive combination for distinguishing serpentinite rocks from their associated talc carbonates and pillowed basalts, as illustrated in Fig. 6. This underscores the effectiveness of PRISMA in addressing intricate geological challenges, thanks to its comprehensive spectral coverage. However, the separation of volcaniclastic metasediments, representing the mélange matrix, from neighboring rock units proves challenging due to shared spectral signatures. Following meticulous visual interpretation aligned with geological maps and extensive fieldwork, our findings affirm the comparable efficacy of the two datasets in highlighting all exposed rock units. This establishes a robust foundation for the careful delineation of training and testing data points to be utilized by the classifier. Thus, for each class, well-distributed pixels were marked with a number that correlated with the area of each target (Table 2).

To recap our methodology, we ensured a perfect geometric correlation between datasets by comparing rock unit pixels. Points for training and testing the random forest model were carefully chosen based on their representation of rock unit variability and to mitigate spatial autocorrelation. These positions were determined using interpretations of previous image processing and field observations. Both datasets and points shared the same geometry. Then, We utilized Python scripts to implement the KCV classification using RF algorithm. The steps of our approach are systematically outlined in a flowchart methodology presented in Fig. 7.

3.4. Random Forest

The Random Forest ensemble classifier has gained widespread acceptance in the field of remote sensing data analysis. As the name implies, the "forest" is a metaphor for a group of Classification and Regression Trees (CARTs) used in prediction (Breiman, 2001). Each tree operates independently, producing unique predictions for every data point. The results, that is, the class probability allocations, are then averaged and combined from all the trees to arrive at a collective judgment. The final label for the supplied data point is this combined judgment. Then, another unlabeled data point for label prediction is fed into the system. A Random Forest's tree count, which is a user-specified parameter, might varies between applications according to the topic, the expected goals, and the data's properties. In a similar vein, users can adjust the tree splitting settings to improve prediction accuracy. Previous studies have shown that the factors controlling tree growth and splitting have a greater impact on Random Forest accuracy than the total number of trees (Belgiu and Drăgu, 2016).Therefore, special attention

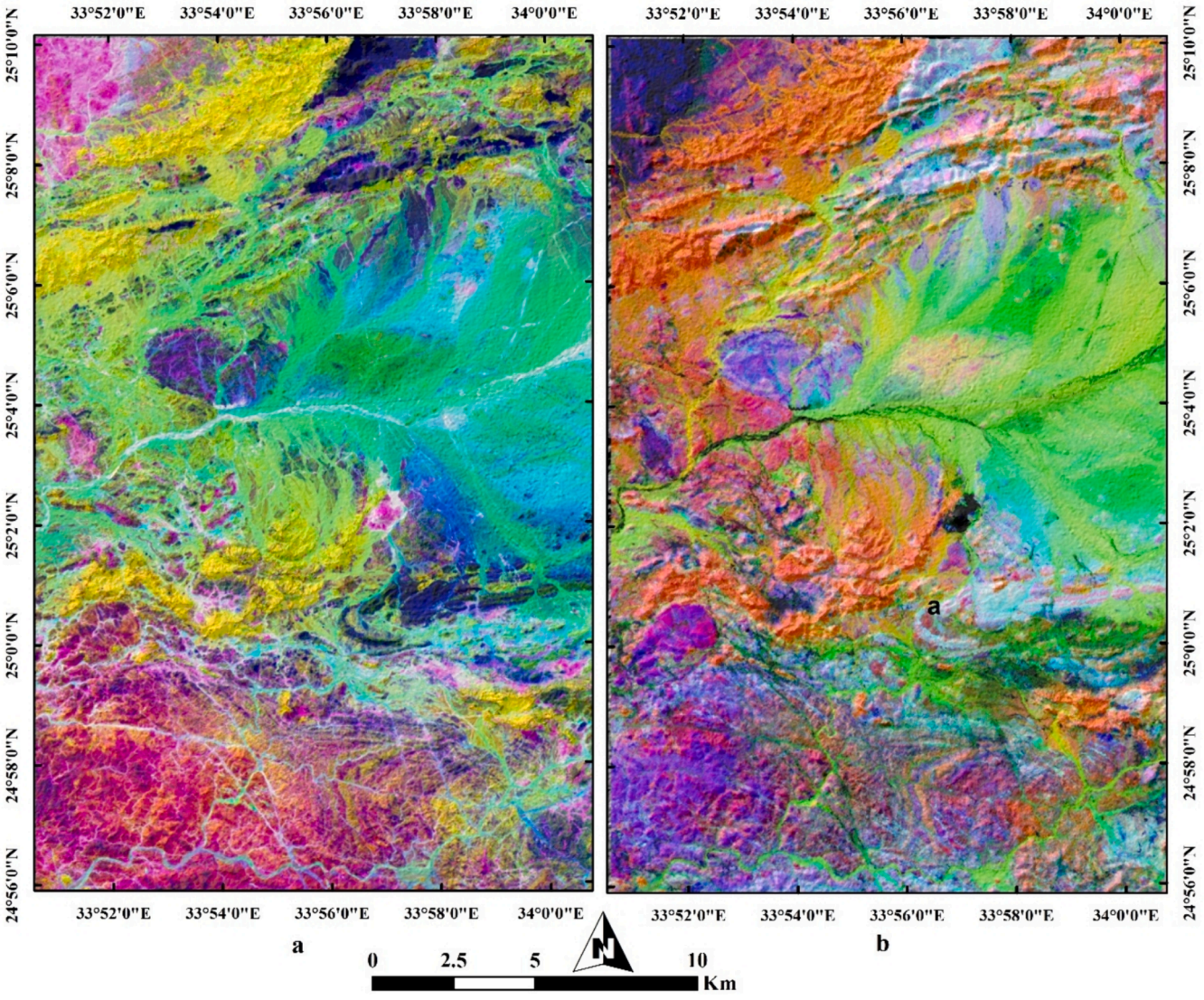

Fig. 4. Lithological discrimination illustrated through PCA: (a) Utilizing RGB channels with Landsat 9 PCs of 3–2-1, and (b) PRISMA PCs of 1–3–2 in RGB, respectively.

was devoted to optimizing the selection of parameters. This meticulous process aimed to achieve enhanced classifier performance and facilitate a more robust comparison across the utilized datasets.

3.5. K fold cross validation (CV)

In comparison to train-test-split approaches, CV is considered to be a more reliable method that offers a more robus error assessment. This is due to the fact that the model undergoes training not exclusively on a singular dataset and subsequent testing on another; rather, it undergoes training on k distinct permutations of data, undergoing independent testing for each of these k iterations. This methodology ensures a more nuanced and comprehensive evaluation of model performance. The CV algorithm computes the cross-validation error, which corresponds to the model's testing error, and then averages this error across all k iterations.

As a method for predictive assessment, cross-validation demonstrates exceptional adaptability due to the wide range of predictive metrics it can accommodate (Gneiting and Raftery, 2007), the array of data-partitioning strategies that can be employed to account for data structure and/or to address computational expenses and estimation bias (Arlot, 2008), and its widespread applicability to both optimization and Bayesian frameworks.

3.6. Grid search method

Various algorithms for tuning hyperparameters are employed to efficiently, rapidly, and reliably identify the optimal combination of model hyperparameters (Bowes et al., 2019). GridsearchCV method, a common hyperparameter optimization technique, was utilized in the current research to identify the optimal values for hyperparameters that yield the best prediction results from the utilized Random Forest model. Grid Search explores various combinations of the specified hyperparameters and their values, assessing the performance of each combination to determine the best values for the hyperparameters. This results in a time-consuming and resource-intensive process.

3.7. Model selection and evaluation

A major concern in model selection is the challenge of overfitting, which involves the inclusion of extraneous variables. Overfitting can misguide research and result in several catastrophic complications in various applications. For predictive goals, overfitting hinders a model's ability to generalize to new data. In cross-validation-based model selection, an efficient strategy involves using calibrated selection rules to identify the simplest model with comparable predictive performance to

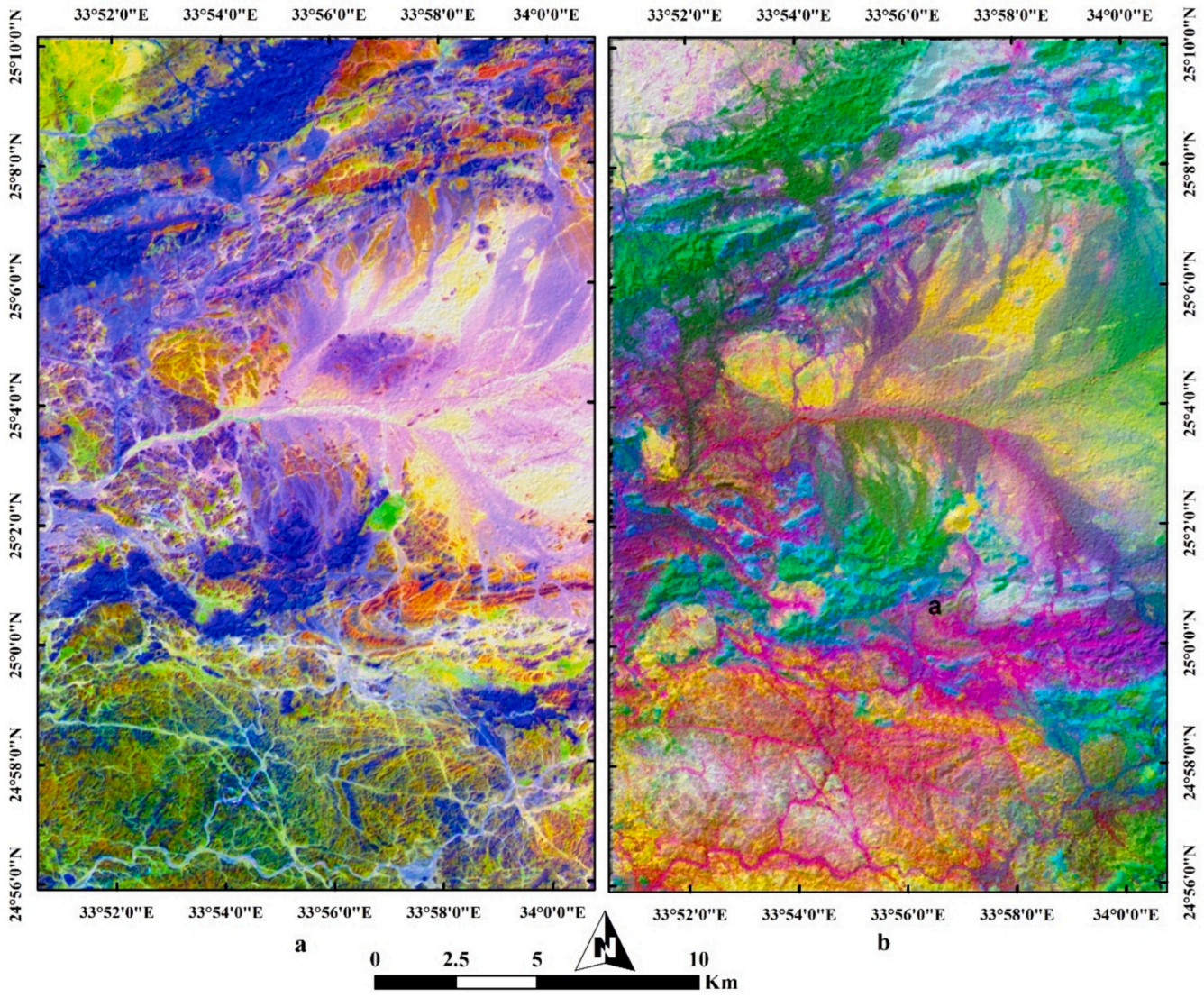

Fig. 5. Lithological discrimination illustrated through image transformations: (a) Utilizing RGB channels with Landsat 9 MNF1-PC1-MNF2, and (b) PRISMA MNF4-MNF6-MNF7 in RGB, respectively.

the top-scoring model (Yates et al., 2021; Yates et al., 2023). For the current research and for each group of the optimum parameters the average accuracy of the models resulting from each folding process was selected.

4. Results

As implied by its name, 'max_depth' governs the maximum depth of each decision tree within the random forest. In our research, this parameter was systematically varied across the values of 'None', 3, 5, 7, 10, 20, 30. Concurrently, 'max_features' dictates the upper limit on the number of features considered for node splitting and was configured with options such as 'None', 'sqrt', and 'log2'. This strategic consideration of these critical parameters aimed to strike a balance between model complexity and computational efficiency.

The heat maps representing the best parameters and their corresponding lithological map were introduced for 2F, 5F, and 10F CV for both Landsat 9 and PRISMA in Fig. 8: 13. As shown in Fig. 8, a total of 21 experiments were meticulously conducted, exploring diverse parameter configurations for max_depth and max_features to ascertain optimal values and identify the most effective Random Forest (RF) algorithm model for both datasets.

Scrutiny of these parameters, in conjunction with their corresponding thematic maps, affirmed the preeminence of a 'max_depth' value of 10 across all folds (2, 5, 10) when utilizing Landsat 9. However, the optimal setting for the maximum features is contingent upon the number of folds. Notably, in the 2-fold (Fig. 8a and 9a) and 5-fold (Fig. 10a and 11a) cross-validation tests, 'sqrt' and 'log2' emerged as judicious choices, delivering reasonable lithological maps. Conversely, as the folds expanded to 10 (Fig. 12a and 13a), designating 'max_features' as 'none' yielded robust outcomes. These findings underscore the adaptive nature of optimal hyperparameter selection based on the intricacies of the dataset folds.

In contrast, when leveraging PRISMA hyperspectral data, it becomes apparent that the 'max_features' parameter has a strong influence on the process compared to 'max_depth', particularly evident for a lower number of folds. Notably, setting 'max_features' to 'None' consistently yields commendable results irrespective of the 'max_depth' value, a phenomenon especially prominent in 2-fold (Fig. 8b and 9b) and 5-fold (Fig. 10b and 11b) cross-validation scenarios. However, as the folds escalate, such as in the case of 10-fold cross-validation (Fig. 12b and 13b), the optimal 'max_features' value shifts to 'sqrt', reflecting an adaptation to increased data partitioning. It is crucial to underscore that optimal outcomes can be attained by adhering to lower 'max_depth'

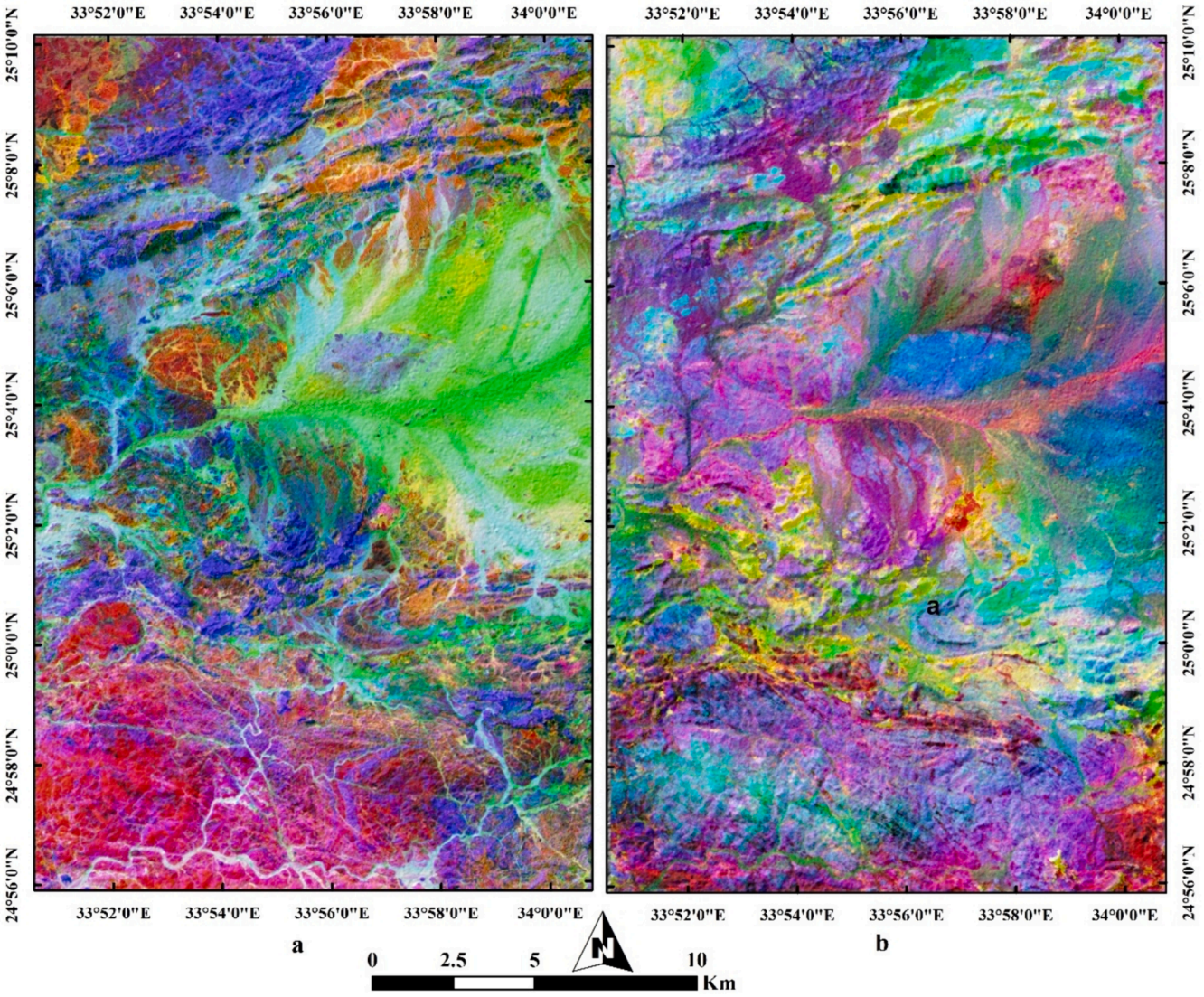

Fig. 6. Lithological discrimination illustrated through image transformations: (a) Utilizing RGB channels with Landsat 9 IC3-IC1-IC2, and (b) PRISMA MNF8- MNF7-MNF9 in RGB, respectively.

values when dealing with a reduced number of data folds. Conversely, increasing 'max_depth' values prove advantageous when the dataset undergoes further subdivision into additional folds. This adjustment underscores the intricate interplay between hyperparameter settings and the intricacies of the hyperspectral dataset, ultimately leading to more refined and robust findings.

Overall, the hyperparameter tuning revealed distinct insights based on the type of the data analysis. When engaging in multispectral data analysis, exemplified by Landsat 9, a discernible correlation emerged with max_depth values. Conversely, the utilization of PRISMA data underscored the pivotal role played by the max_features parameter. Examination of the lithological targets in the resulting thematic maps from both Landsat 9 and PRISMA, particularly when utilizing a reduced training dataset, such as in the case of 2-fold cross-validation (2F CV), reveals a notable proliferation of error pixels. A striking example lies in the depiction of Metagabbro Diorite rocks (MGD), where Landsat 9 output (Fig. 9a) exhibits an unrealistic exaggeration and expansion compared to the more accurate representation in PRISMA (Fig. 9b). Similarly, an examination of volcaniclastic metasediments (VMs) in the lower part of the map exposes a prevalence of error pixels, predominantly in yellow hues, for Landsat 9 in contrast to the more precise mapping achieved by PRISMA. Further scrutiny reveals that these yellow pixels, ostensibly indicating artisanal mining activities, are misallocated along the volcaniclastic metasediments in both datasets using 2F CV. Landsat 9 exhibits an excessive distribution, while PRISMA introduces a considerably less accurate representation of the true distribution of these artisanal works. Consequently, this discrepancy prompted an additional dataset splitting into additional folds, a strategic measure to augment the utilization of available training points. The aim is to empower the classifier in constructing a more robust model for accurate lithological predictions, addressing the challenges posed by the intricate distribution patterns observed in the initial evaluations using 2F CV.

In the case of 5-fold cross-validation (5F CV), clearly superior results are shown in Fig. 11a and 11b. The utilization of 5F CV achieves a more precise allocation of all rock units compared to the previous 2-fold CV, albeit with residual errors. Notably, the distribution of Metagabbro Diorite rocks (MGD) persists as more exaggerated in Landsat 9, and some error pixels still affect the precision of PRISMA's findings, particularly evident in the unrealistic distribution of yellow pixels within acidic metavolcanics (MVs).

To address these persistent challenges, we further partitioned the datasets into 10 folds. This deliberate move sought to significantly enhance the classifier's potential by affording it greater opportunities to

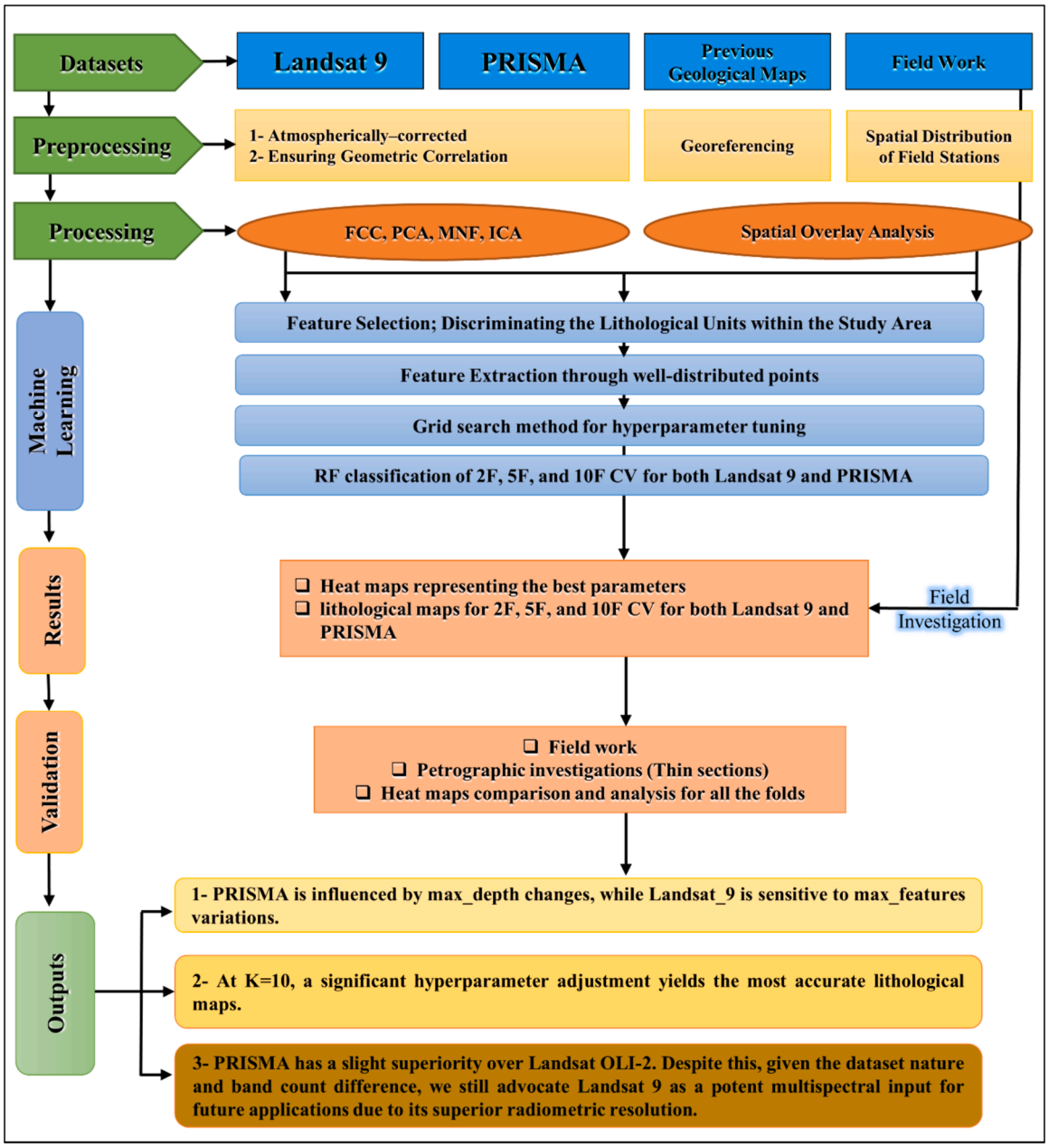

Fig. 7. Flow chart illustrating the methodology adopted in the current study.

leverage an increased number of training points. The outcomes of the 10-fold CV, as depicted in Fig. 13a and 13b, stand out as the pinnacle findings in the current research for both Landsat 9 and PRISMA. Despite minor variations in the distribution of lithological targets, PRISMA data consistently outshines with more accurate predictions. For instance, in the northwestern part of the map in the PRISMA thematic representation, talc carbonates (TC) are sensibly concentrated around serpentinite rocks, aligning with geological expectations. Conversely, Landsat 9 exhibits a notably subdued representation of TC in the same area. Similarly, the distribution of acidic metavolcanics at the southwestern corner of the map appears more faithfully represented in PRISMA, showcasing the model's heightened accuracy compared to Landsat 9.

Overall, the generalized lithological maps (Figs. 9, 11, and 13) showed consistent acceptability across both datasets and varied fold configurations, underscoring the efficacy of GridSearch CV in pinpointing optimal parameters tailored to each case, accounting for both dataset characteristics and fold variations. While subtle distinctions surfaced in the predictive maps between Landsat 9 and PRISMA, even with identical fold settings, both outputs held merit and validity upon meticulous comparison with prior geological maps and on-site investigations. Importantly, our findings revealed that PRISMA's lithological predictions exhibit superior precision when juxtaposed with Landsat 9 (Figs. 9, 11, and 13).

5. Field verification

Our research involved extensive fieldwork to investigate the rock units in the study area and validate our findings regarding the thematic maps. In particular, there was significant agreement between our results, particularly where K = 10, and the results of the fieldwork. For instance, Metagabbroic rocks, identified as having varying grain sizes and displaying mesocratic or melanocratic colors (Fig. 14a), were distributed across different regions of the study area. Additionally, serpentinites and talc-carbonate rocks (Fig. 14b) were noticed amidst a mix

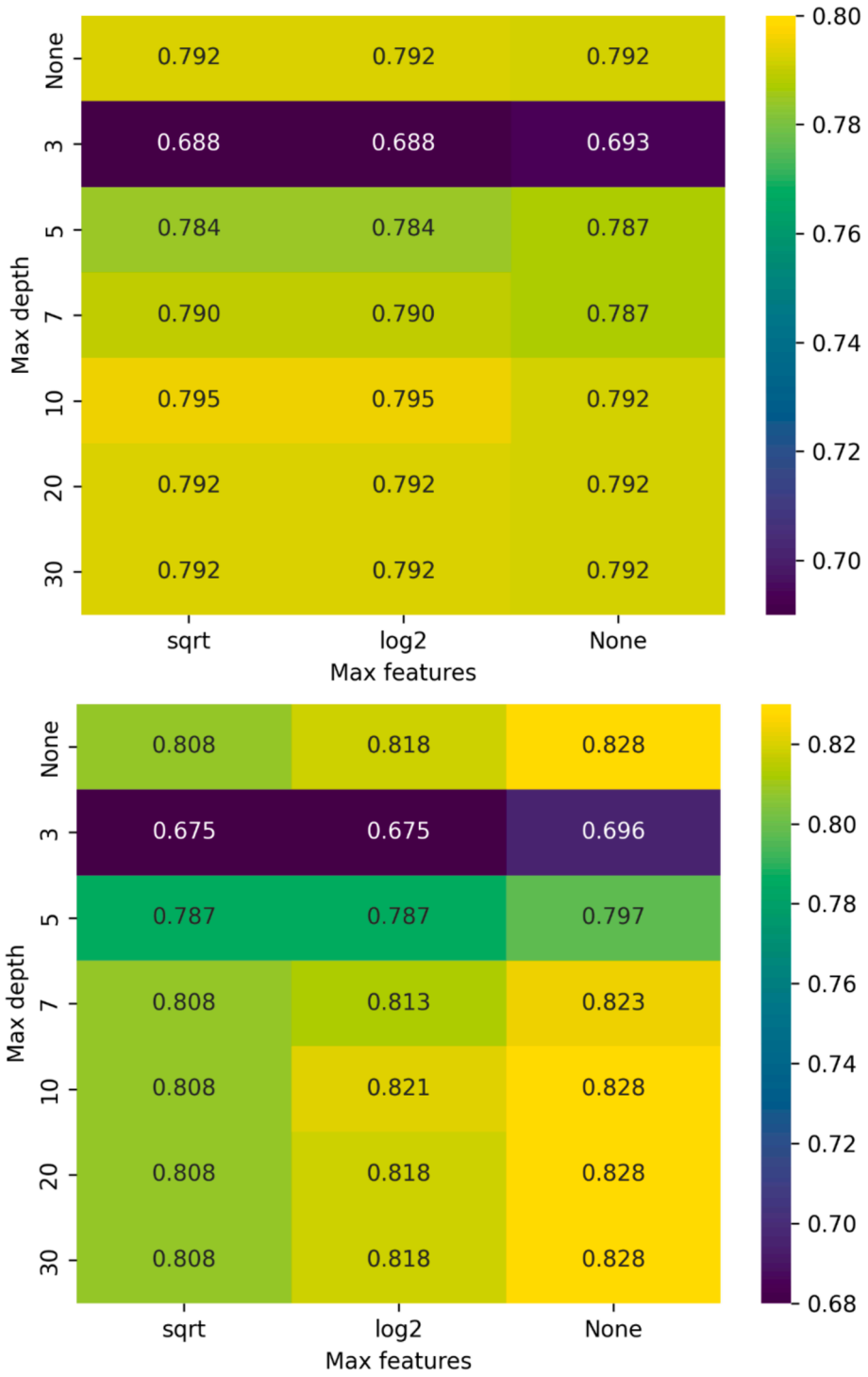

Fig. 8. Presents a heat map showcasing diverse hyperparameter tuning outcomes during 2-fold cross-validation for (a) landsat 9, and (b) prisma data. light yellow tones indicate superior scores.

of volcaniclastic metasediments (Fig. 14 b-d), representing the ophiolitic mélange matrix within the study area.

Within the study area, the mélange matrix, composed predominantly of quartzofeldspathic schists, exhibited a well-defined preferred orientation (Fig. 14 c, d), trending NW-SE to E-W, and predominantly dipping towards the north. A substantial portion of the studied terrain is covered by an island arc association, primarily consisting of metavolcanic rocks (Fig. 14 d, e) exposed in the southwestern part of the study area. Notably, these rocks serve as the host for the Dungash gold deposit, a vein-type gold deposit located in the southwestern part of the study area. The island arc assemblage within the studied terrain comprises metamorphosed (mostly greenschist facies) basic-intermediate metavolcanics, including basaltic andesite to basalt and inferior dacites, as well as pyroclastic tuffs/breccias (Zoheir and Weihed, 2014). Accurate delineation of the distribution of these rocks holds the potential to provide valuable insights into the extent of host rocks for mineralization, thereby offering economic benefits.

Our petrographic analysis revealed that the exposed serpentinites in the study area are predominantly composed of antigorite, with observed opaques represented by iron oxides. Talc and calcite are frequently

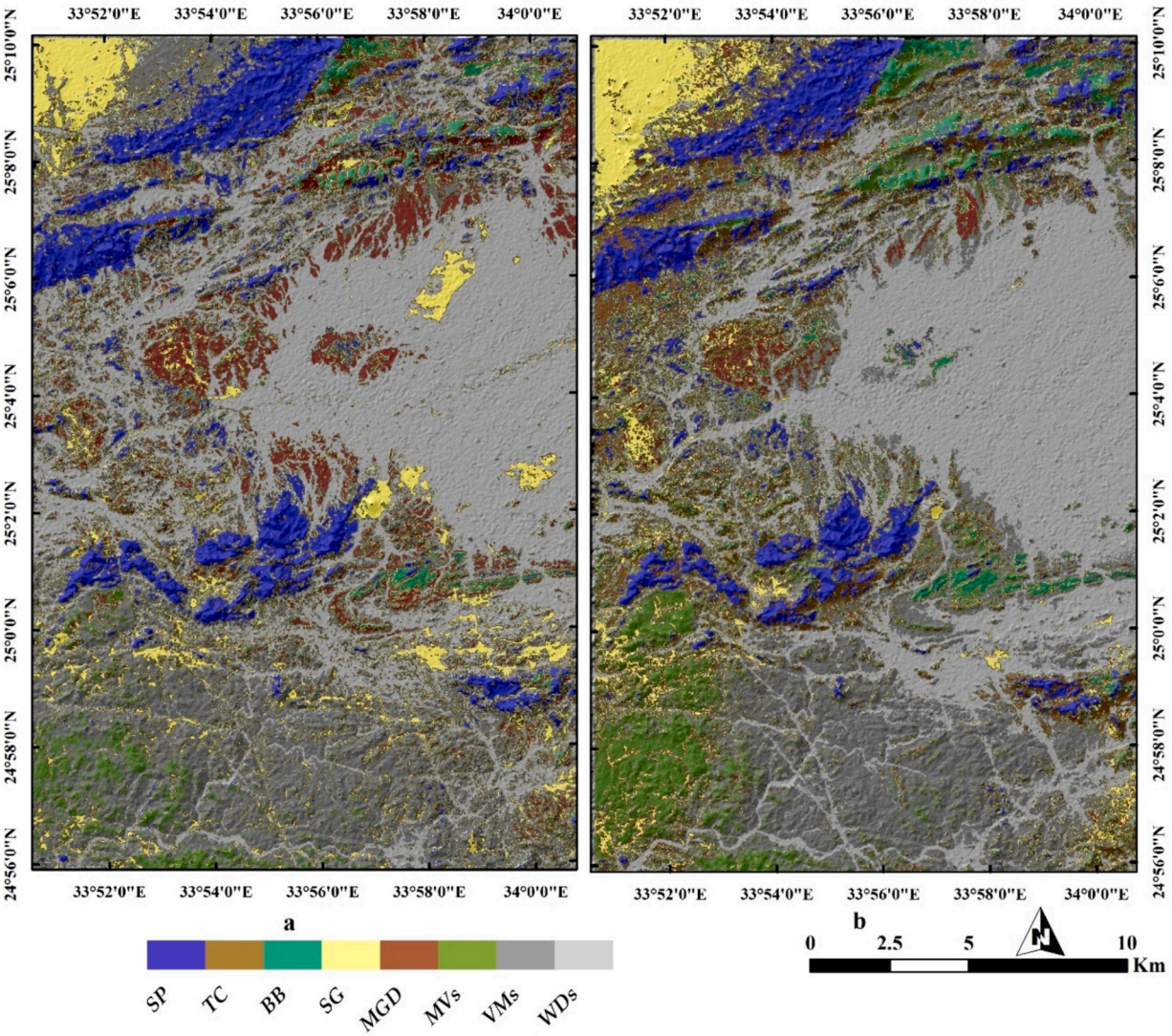

Fig. 9. Lithological maps generated through Random Forest with 2-fold CV using (a) Landsat 9 and (b) PRISMA data.

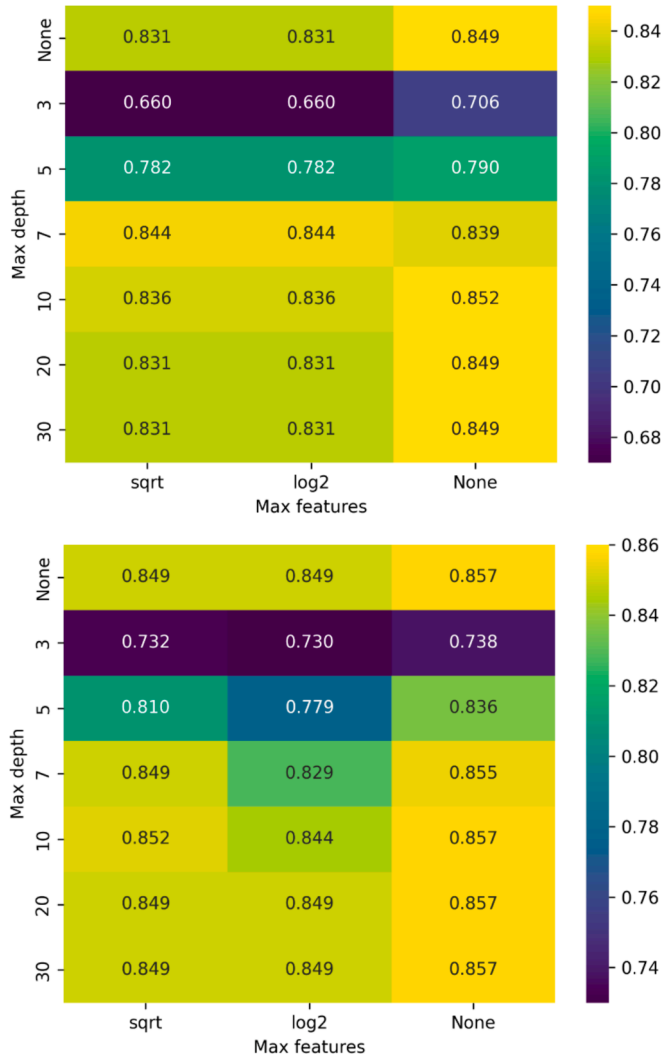

Fig. 10. Presents a heat map showcasing diverse hyperparameter tuning outcomes during 5-fold cross-validation for (a) landsat 9, and (b) prisma data. light yellow tones indicate superior scores.

observed, particularly in association with talc carbonate rocks (Fig. 15a). Metagabbroic rocks present a distinctive greyish-green appearance speckled with white. These rocks primarily consist of highly saussuritized plagioclase, hornblende, tremolite-actinolite, epidote, clinozoisite, calcite, sericite, and chlorite (Fig. 15b). The mélange matrix is composed of quartz-feldspathic schists (Fig. 15c-f). True to their name, these rocks are primarily composed of quartz and plagioclase (Fig. 15c-f), with accessory opaques displaying a noticeable schistosity.

Metavolcanic rocks, mainly Meta-andesites, contain minerals such as plagioclase, chlorite, epidote, hornblende, and alkali-feldspars in their groundmass (Fig. 16a-d). Within all metavolcanic varieties, plagioclase crystals show varying degrees of alteration. This alteration is evident across all rock units exposed in the studied terrain, including meta gabbro-diorite rocks in Fig. 16e and f, reflecting the complex deformational tectonic history and the influence of hydrothermal fluids responsible for enriching gold deposits within the study area, characterized as orogenic gold deposits.

6. Discussion

Among several available MLAs, the current research applied random forests (feature bagging algorithm), a type of bagging, that uses decision trees with a random selection of features (Gewali et al., 2018). Random forest is a category of ensemble learning (Rokach, 2010), a supervised learning methodology, that amalgamates the predictions of multiple base models to enhance overall accuracy. To optimize results, diversity, and lack of correlation among base predictors (e.g., decision trees) are imperative in ensemble learning techniques. This approach has proven particularly effective in hyperspectral image classification (Gewali et al., 2018; Shebl et al., 2023a). The accuracy of the resulting thematic maps is significantly influenced not only by the specific characteristics of the employed data and predictive approach of the algorithms but also by the fine-tuning of hyperparameters. In the present work, this phenomenon was highlighted and investigated using PRISMA and Landsat 9 datasets focusing mainly on ‘max_depth‘ and ‘max_features‘ as the main parameters with random forests (Contreras et al., 2021; Nadi and Moradi, 2019).

The maximum depth of individual trees within a random forest, controlled by the ‘max_depth‘ parameter, exerts profound influence. In the context of Landsat 9 data analysis, increasing radiometric resolution adds complexity to the feature space. The current reasonable findings from Landsat 9 illustrate that deeper trees have the potential to discern intricate data patterns, culminating in commendable generalization. This may reflect the potential of Landsat 9 data in further future applications e.g. vegetation indices or texture features analysis. Nonetheless, an unbridled increase in ‘max_depth‘ may induce overfitting, where the model adapts to the noise inherent in the training data.

In our research, this phenomenon becomes clear and better explained by examining the hyperparameter heat maps associated with Landsat 9. Notably, adopting ‘max_depth‘ values of 2 and 5 (Fig. 7a and 9a) consistently yields diminished accuracy across diverse ‘max_features‘ parameters. This disparity can be ascribed to the creation of shallow trees that inadequately encapsulate the intricate relationships embedded in the data. Amplifying the number of folds (e.g., k = 10) augments the impact of a slight increase in ‘max_depth‘ (e.g., 7), resulting in an increase in accuracy and the production of reasonable thematic maps. A pronounced elevation of ‘max_depth‘ to 10 emerges as the optimum value across all conducted experiments employing Landsat 9 (Fig. 11a). Any ‘max_depth‘ value above 10 entails an escalating intricacy, potentially causing overfitting—a scenario where the random forest model captures training data noise that resist reasonable generalization to unseen data.

A careful examination of heat maps spanning various folds confirms that the peak of generalization is reached at ‘max_depth‘ = 10. Beyond this threshold (e.g., 20 or 30), no discernible enhancement in the generalization process transpires; instead, it begets an excessively profound tree, thereby compromising generalization to unseen data, while concurrently escalating computational demands. Our findings align with earlier research that asserts, irrespective of the number of informative features, the classification accuracy reaches a plateau beyond a certain tree depth (10 in our case) (Nadi and Moradi, 2019).

The ‘max_features‘ parameter dictates the utmost number of features considered when splitting a node in a tree. As hyperspectral data has an increasing number of bands, the model confronts a richer set of information at each bifurcation. Allowing the model to consider a wider range of features prove advantageous, particularly in the presence of abundant spectral data. This facilitates the model in harnessing the intricacies afforded by the expanding band count. Nevertheless, the selection of various ‘max_features‘ values—such as None, sqrt, and log2—can exert distinctive influences on algorithmic performance, particularly when applied to PRISMA data, as the effective depth of the trees for a specific dataset is contingent upon the count of effective features being employed (Nadi and Moradi, 2019).

In our study, opting for ‘max_features‘ set to None entails the algorithm considering all PRISMA data features during each split. While this strategy adeptly captures intricate data relationships, fostering improved generalizations, it concurrently escalates computational demands and the peril of overfitting, especially in the context of a modest

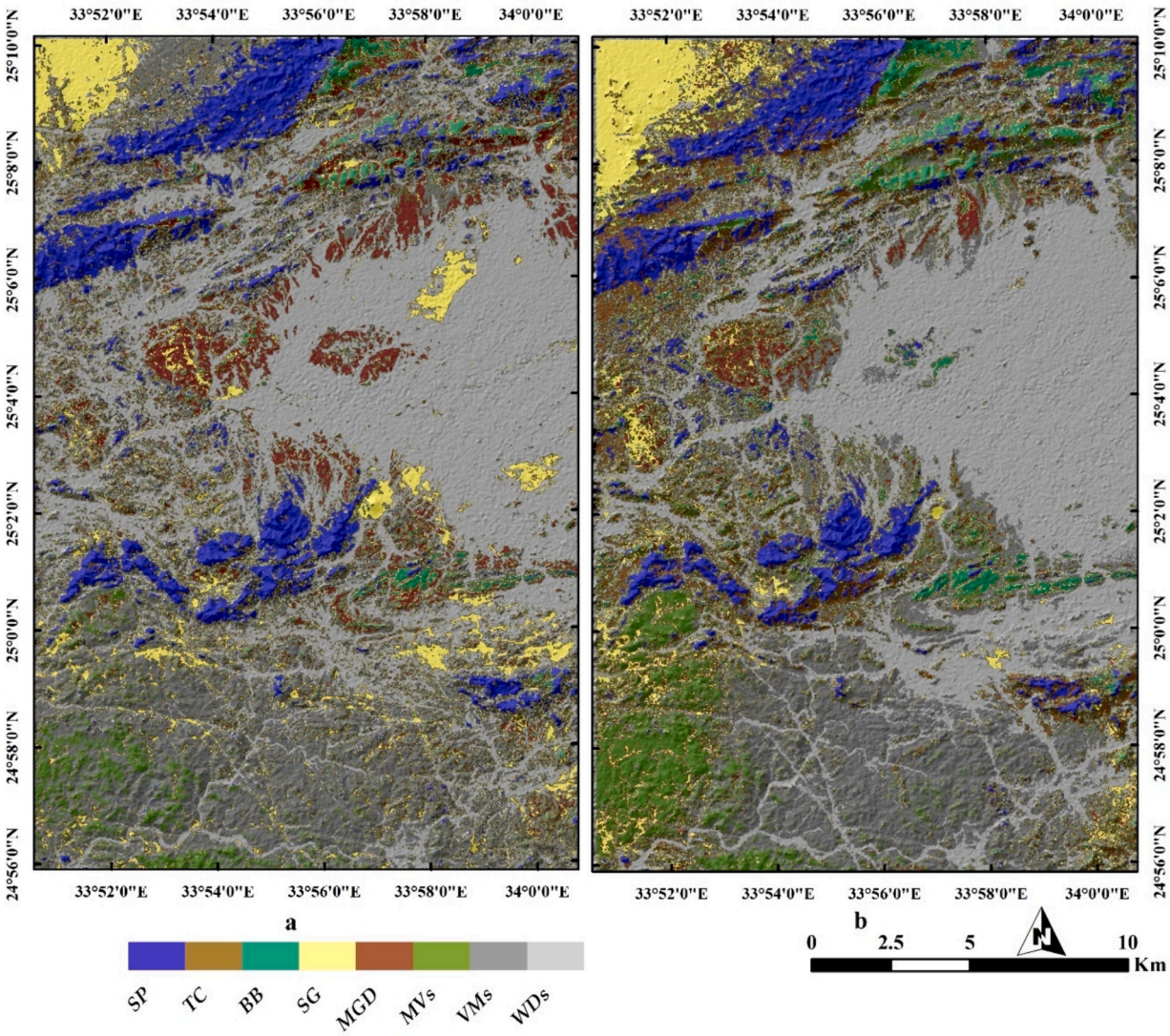

Fig. 11. Lithological maps generated through Random Forest with 5-fold CV using (a) Landsat 9 and (b) PRISMA data.

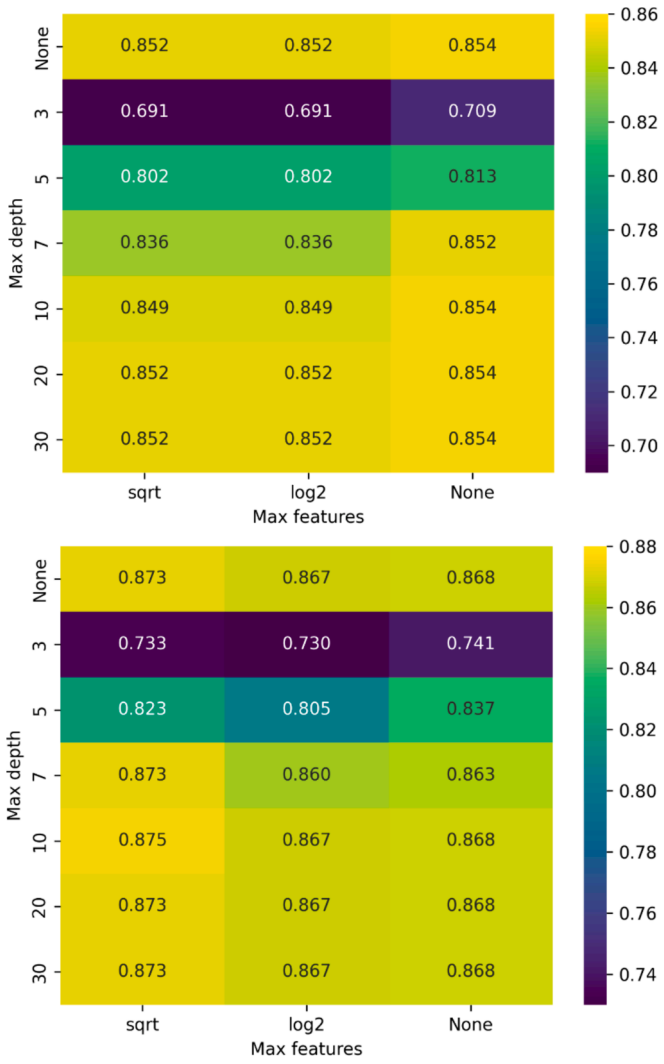

Fig. 12. Presents a heat map showcasing diverse hyperparameter tuning outcomes during 10-fold cross-validation for (a) landsat 9, and (b) prisma data. light yellow tones indicate superior scores.

training dataset. Thus, our research underscores (Fig. 7b and 9b) the recommendation of using "None" when training data volume is constrained (e.g., K = 2 or 5). Employing "None" as the optimal features value demonstrates superior generalization accuracy, constructing intricate relationships, and maximizing data feature utility. This is particularly evident in heat maps, where "None" emerges as the optimal value, especially for k = 2 or 5, when 'max_depth' is set to 10, fostering the creation of sufficiently deep trees for substantial generalizations.

In scenarios where the training data is expanding, reducing the number of features is less critical than in data-sparse situations. For instance, configuring 'max_features' to sqrt involves investigating the square root of total features (approximately 15) per split. The best fit with the sqrt max_features value is achieved with k = 10 striking a harmonious balance between feature subset consideration and averted overfitting risks (Fig. 11b). This configuration empowers the model to exploit spectral richness without overwhelming computational resources.

When 'max_features' is set to log2, only 8 features are considered at each split. However, this manifests as reasonable generalization when k = 10, due to the optimal 'max_depth' and the availability of sufficient training data. This setting limits the number of features considered. Consequently, our research identifies sqrt 'max_features' and a 'max_depth' of 10 as optimal parameters for PRISMA datasets (Fig. 11b and 12b). In the case of Landsat 9 data, the inclusion of all features proves to be crucial for the construction of a deep and complex model. Consequently, the best classification result for Landsat 9 is achieved when both 'max_features' and 'max_depth' are set to None and 10, respectively (Fig. 11a and 12 a)confirming that 'max_depth' effect is influenced by its interaction with the 'max_features' hyperparameter (Contreras et al., 2021). Our research highly recommends adopting both Landsat 9 and PRISMA for several future applications using RF, with special consideration of 'max_features' and 'max_depth' as critical parameters. Additionally, better implementation of hyperparameter tuning methods greatly helps in selecting the best model, resulting in resolving the complexities among the classified targets (e.g., Neoproterozoic rock in the current research).

7. Conclusion

The current study tested two recently launched sensors to assess their performance in lithological mapping using Random Forests and concludes the following findings:

1. Recent advances in the PRISMA hyperspectral sensor and Landsat OLI 2, both offering powerful data with 240 spectral bands and dynamic resolutions, underlined their efficiency in delivering accurate lithological mapping.

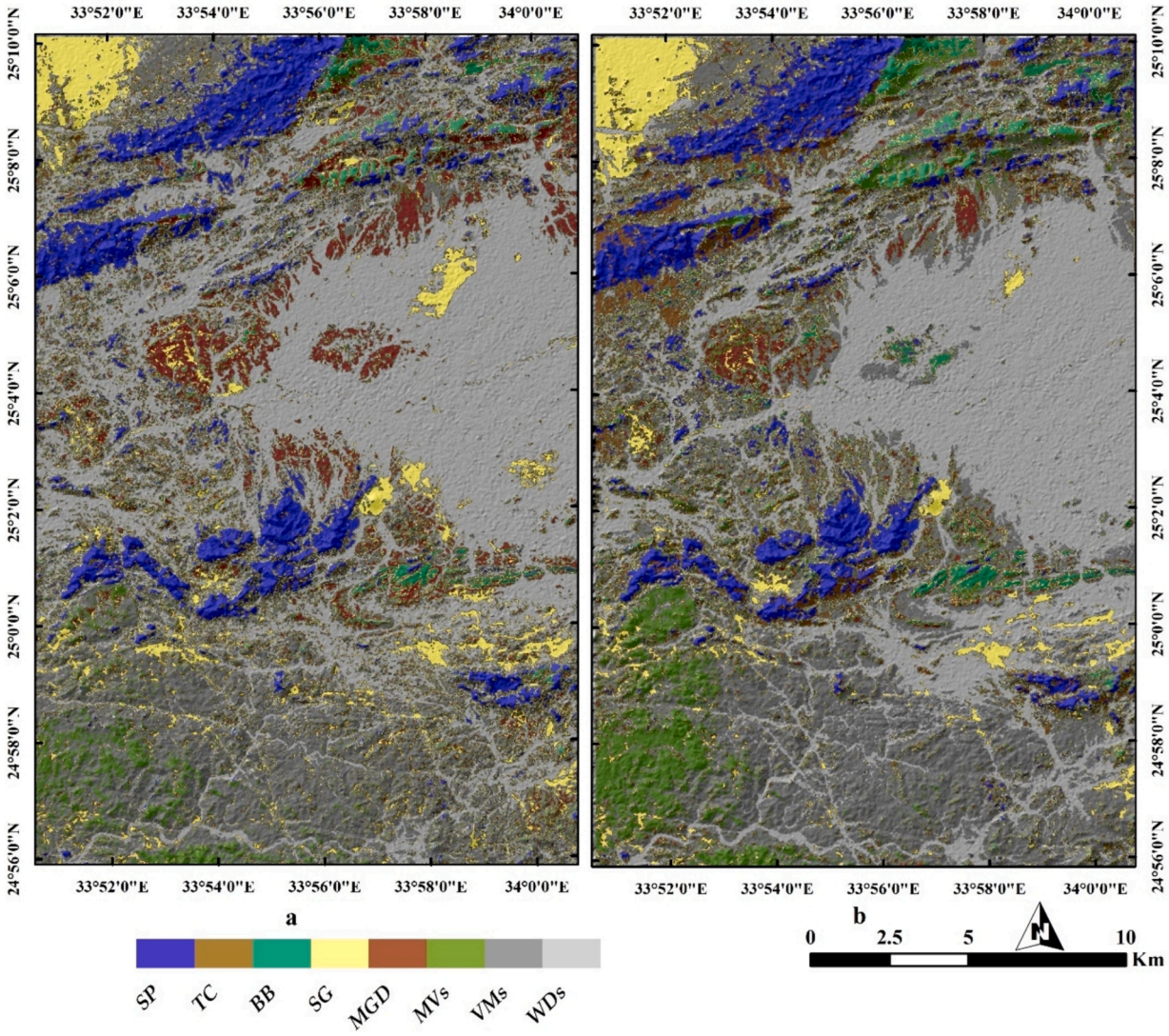

Fig. 13. Lithological maps generated through Random Forest with 10-fold CV using (a) Landsat 9 and (b) PRISMA data.

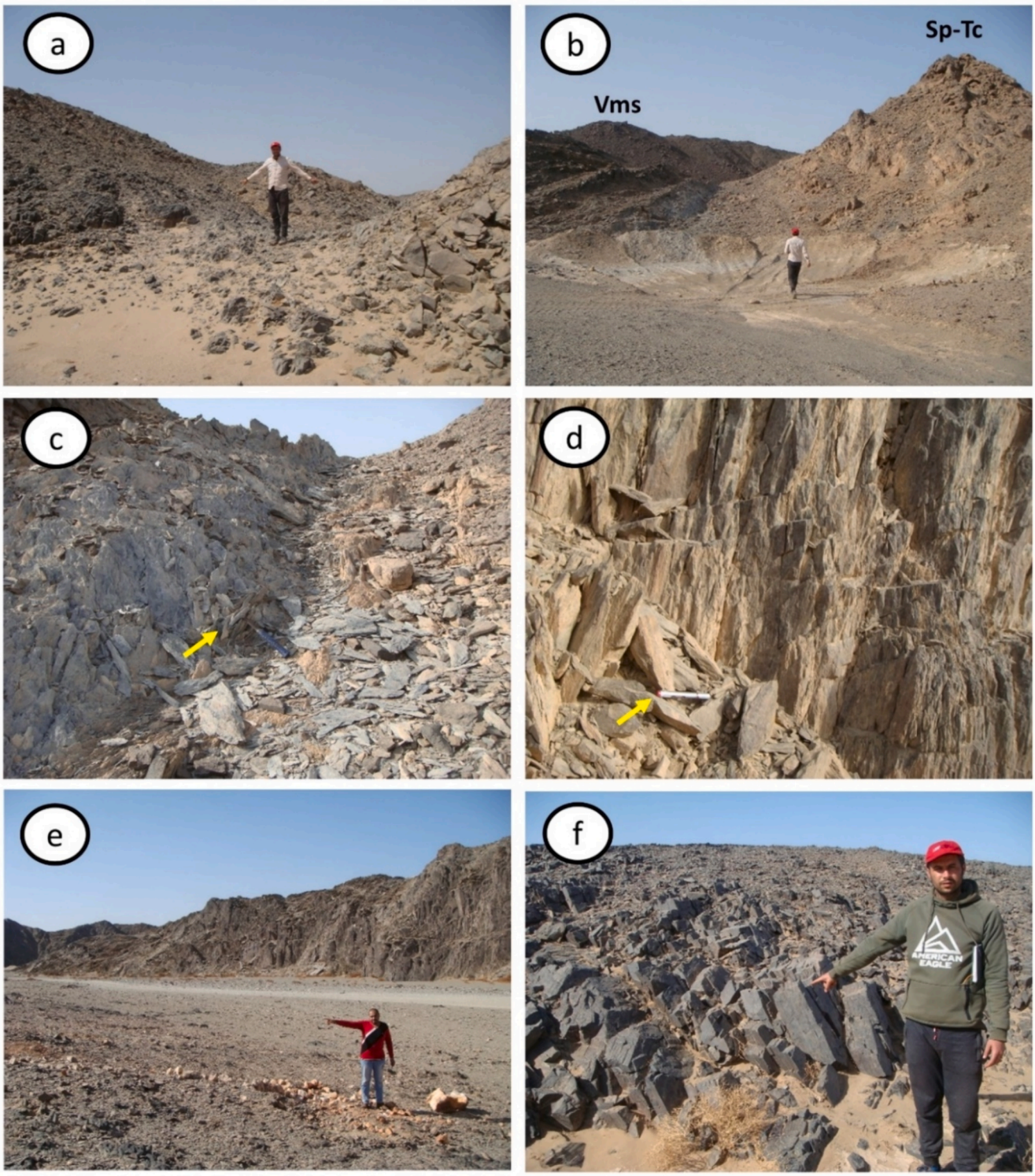

Fig. 14. Field photographs highlighting (a) Low-land metagabbros depicted as heterogeneous blocks, exhibiting subtle variations in color, (b, c, and d) Showcase the ophiolitic melange matrix (b) encompassing fragments of serpentinite-talc carbonate and (c, d) revealing intense shearing and well-developed preferred orientation of these volcaniclastic metasediments. (e) Provides a general perspective of the metavolcanic within the study area, (f) shows highly dissected basaltic *meta*-andesites.

2. A significant dependence between the chosen dataset and hyper-parameters, with PRISMA notably influenced by changes in max_-depth, while Landsat_9 showed sensitivity to variations in max_features.
3. For all K values, our approach yielded reasonable lithological maps with an acceptable degree of accuracy, emphasizing the pivotal role of the grid search method in balancing dataset characteristics and data splitting(affecting the available number of training data points).
4. Validation by fieldwork and petrographic investigations confirmed the accuracy of the resulting thematic maps especially when K = 10.

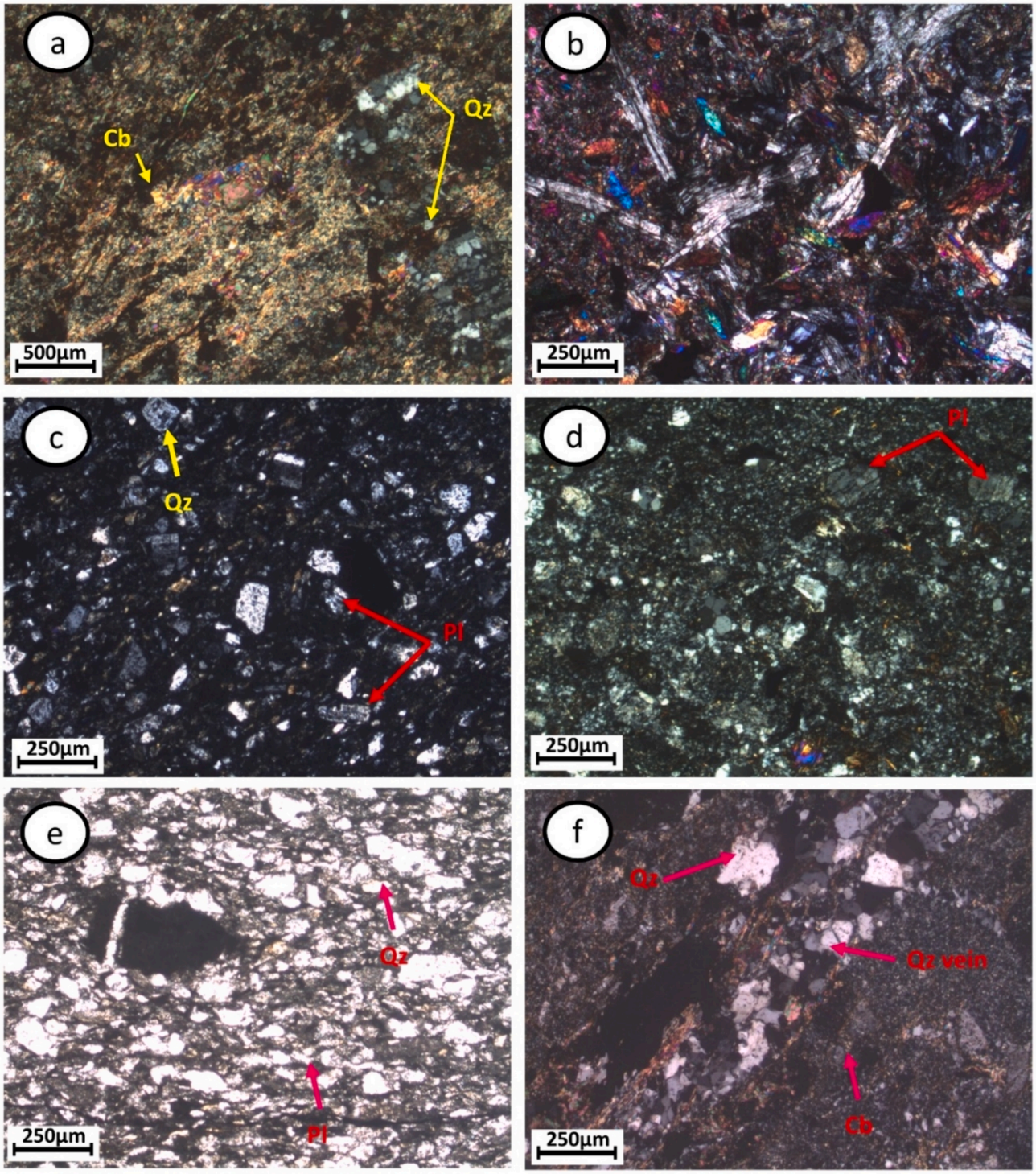

Fig. 15. Photomicrographs showing various petrographic features of (a) serpentinites and their associated carbonates, and (b) metagabbroic rocks. Photomicrographs of (c, d, and e) highlight the main petrographic characteristics of the ophiolitic mélange matrix and displaying a weak schistosity. (f) volcaniclastic metasediments with prominent quartz crystals are cut by a quartz vein, set within a fine-grained carbonate-rich schistose matrix. All photos are taken in cross-polarized transmitted light (CN), except panel (e) is under plane-polarized light (PPL). (Cb: carbonate, Pl:plagioclase, Qz:quartz).

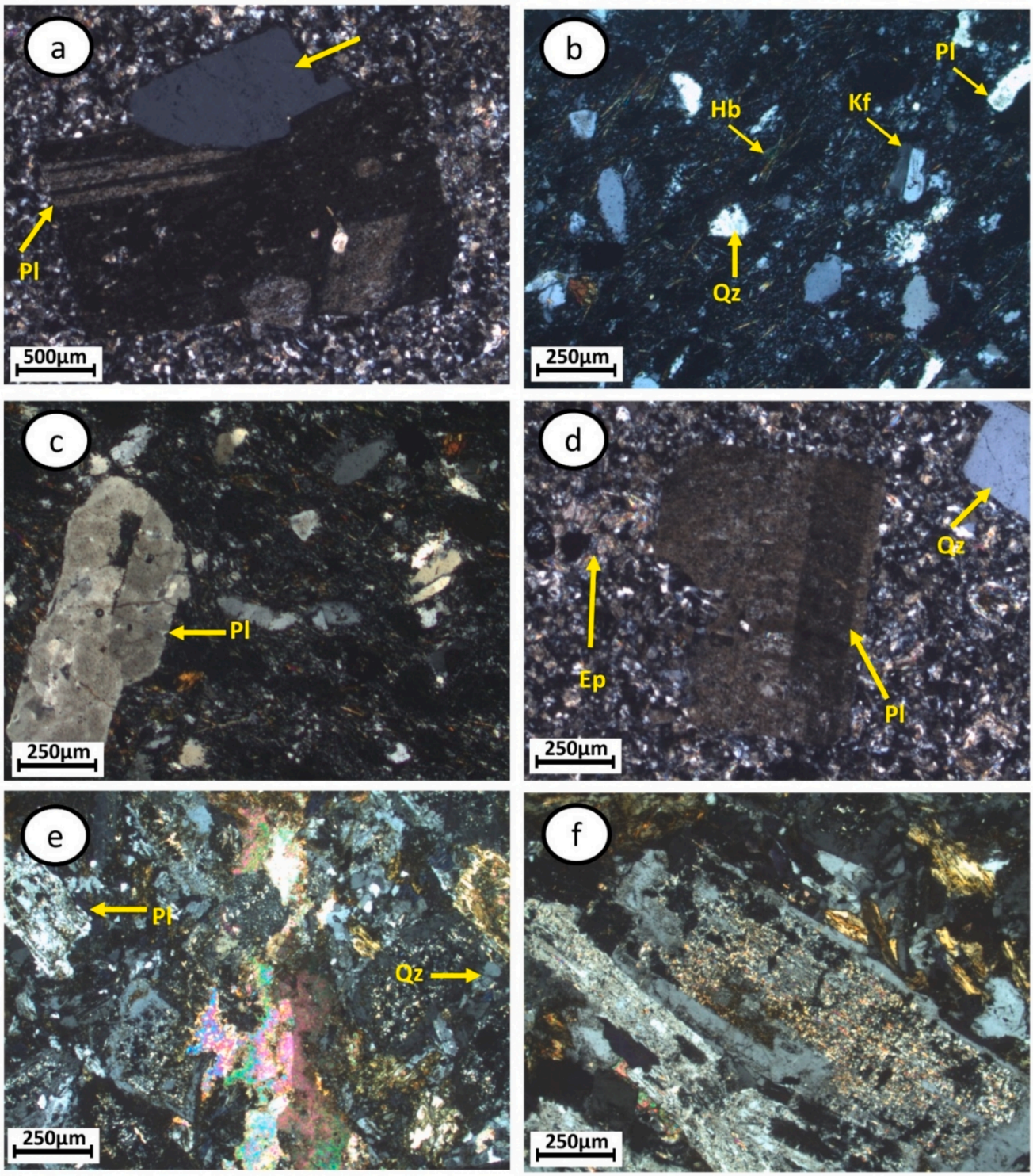

Fig. 16. (a, b, c and d) Photomicrographs showing the primary petrographic characteristics of metavolcanics demonstrating porphyritic textures, predominantly composed of plagioclase and quartz phenocrysts embedded in a finely-grained groundmass. (e, and f) Photomicrographs revealing the key petrographic features of meta gabbro-diorite rocks and showing highly sassuritized plagioclase, resulting from hydrothermal alteration of the original plagioclase feldspar. All photos are taken in cross-polarized transmitted light (CN). (Pl:plagioclase, Qz:quartz, Ep: Epidote).

CRediT authorship contribution statement

Ali Shebl: Conceptualization, Investigation, Methodology, Validation, Visualization, Writing – original draft, Writing – review & editing. **Dávid Abriha:** Conceptualization, Data curation, Methodology, Resources, Visualization, Writing – review & editing. **Maher Dawoud:** Formal analysis, Investigation. **Mosaad Ali Hussein Ali:** Formal analysis, Investigation. **Árpád Csámer:** Conceptualization, Methodology, Supervision.

Declaration of Competing Interest

The authors declare that they have no known competing financial interests or personal relationships that could have appeared to influence the work reported in this paper.

Acknowledgement

The research was financed by the NKFI K138079.

References

Abdelsalam, M.G., Stern, R.J., 1996. Sutures and shear zones in the Arabian-Nubian Shield. J. African Earth Sci. 23, 289–310.

Abriha, D., Srivastava, P.K., Szabó, S., 2023. Smaller is better? Unduly nice accuracy assessments in roof detection using remote sensing data with machine learning and k-fold cross-validation. Heliyon 9. https://doi.org/10.1016/j.heliyon.2023.e14045.

Alibrahim, H., Ludwig, S.A., 2021. Hyperparameter optimization: Comparing genetic algorithm against grid search and bayesian optimization. In: In: 2021 IEEE Congress on Evolutionary Computation (CEC), pp. 1551–1559.

Al-Ruzouq, R., Shanableh, A., Jena, R., Mukherjee, S., Khalil, M.A., Gibril, M.B.A., Pradhan, B., Hammouri, N.A., 2024. Hybrid deep learning and remote sensing for the delineation of artificial groundwater recharge zones. Egypt. J. Remote Sens. Sp. Sci. 27, 178–191.

Aneece, I., Thenkabail, P.S., 2022. New Generation Hyperspectral Sensors DESIS and PRISMA Provide Improved Agricultural Crop Classifications. Photogramm. Eng. Remote Sensing 88, 715–729. https://doi.org/10.14358/PERS.22-00039R2.

Anguita, D., Ghelardoni, L., Ghio, A., Oneto, L., Ridella, S., others, 2012. The'K'in K-fold Cross Validation., in: ESANN. pp. 441–446.

Arlot, S., 2008. V-fold cross-validation improved: V-fold penalization. arXiv Prepr. arXiv0802.0566.

Bahrami, H., Esmaeili, P., Homayouni, S., Pour, A.B., Chokmani, K., Bahroudi, A., 2024. Machine Learning-Based Lithological Mapping from ASTER Remote-Sensing Imagery. Minerals 14, 202.

Bedini, E., Chen, J., 2022. Application of PRISMA satellite hyperspectral imagery to mineral alteration mapping at Cuprite, Nevada, USA. J. Hyperspectral Remote Sens. 124–130.

Belgiu, M., Drăgu, L., 2016. Random forest in remote sensing: A review of applications and future directions. ISPRS J. Photogramm. Remote Sens. 114, 24–31. https://doi.org/10.1016/J.ISPRSJPRS.2016.01.011.

Bhat, S.S., Ansari, G.A., Ansari, M.D., 2024. Performance Analysis of Machine Learning Based On Optimized Feature Selection for Type II Diabetes Mellitus. Multimed. Tools Appl. 1–20.

Bowes, B.D., Sadler, J.M., Morsy, M.M., Behl, M., Goodall, J.L., 2019. Forecasting groundwater table in a flood prone coastal city with long short-term memory and recurrent neural networks. Water 11, 1098.

Breiman, L., 2001. Random Forests. Mach. Learn. 451 (45), 5–32. https://doi.org/10.1023/A:1010933404324.

Burman, P., 1989. A comparative study of ordinary cross-validation, v-fold cross-validation and the repeated learning-testing methods. Biometrika 76, 503–514.

Chacón, J., Irigaray, C., Fernández, T., El Hamdouni, R., 2006. Engineering geology maps: landslides and geographical information systems. Bull. Eng. Geol. Environ. 65, 341–411. https://doi.org/10.1007/s10064-006-0064-z.

Chang, Q., Ruan, Z., Yu, B., Bai, C., Fu, Y., Hou, G., 2024. Data-Driven Classification and Logging Prediction of Mudrock Lithofacies Using Machine Learning: Shale Oil Reservoirs in the Eocene Shahejie Formation, Bonan Sag, Bohai Bay Basin. Eastern China. Minerals 14, 370.

Chen, L., Guo, Z., Yin, K., Shrestha, D.P., Jin, S., 2019. The influence of land use and land cover change on landslide susceptibility: a case study in Zhushan Town, Xuan'en County (Hubei, China). Nat. Hazards Earth Syst. Sci. 19, 2207–2228. https://doi.org/10.5194/nhess-19-2207-2019.

Chen, Y., Tian, M., Wu, Q., Tao, L., Jiang, T., Qiu, Q., Huang, H., 2024. A deep learning-based method for deep information extraction from multimodal data for geological reports to support geological knowledge graph construction. Earth Sci. Informatics 1–21.

Contreras, P., Orellana-Alvear, J., Muñoz, P., Bendix, J., Célleri, R., 2021. Influence of Random Forest Hyperparameterization on Short-Term Runoff Forecasting in an Andean Mountain Catchment. Atmosphere (basel). 12 https://doi.org/10.3390/atmos12020238.

Dearman, W.R., Fookes, P.G., 1974. Engineering geological mapping for civil engineering practice in the United Kingdom. Q. J. Eng. Geol. 7, 223–256. https://doi.org/10.1144/GSL.QJEG.1974.007.03.01.

Gewali, U.B., Monteiro, S.T., Saber, E., 2018. Machine learning based hyperspectral image analysis: a survey. arXiv Prepr. arXiv1802.08701.

Gholinejad, S., Naeini, A.A., Amiri-Simkooei, A., 2019. Robust Particle Swarm Optimization of RFMs for High-Resolution Satellite Images Based on K-Fold Cross-Validation. IEEE J. Sel. Top. Appl. Earth Obs. Remote Sens. 12, 2594–2599. https://doi.org/10.1109/JSTARS.2018.2881382.

Giardino, C., Bresciani, M., Braga, F., Fabbretto, A., Ghirardi, N., Pepe, M., Gianinetto, M., Colombo, R., Cogliati, S., Ghebrehiwot, S., Laanen, M., Peters, S., Schroeder, T., Concha, J.A., Brando, V.E., 2020. First Evaluation of PRISMA Level 1 Data for Water Applications. Sensors 2020, Vol. 20, Page 4553 20, 4553. https://doi.org/10.3390/S20164553.

Gneiting, T., Raftery, A.E., 2007. Strictly proper scoring rules, prediction, and estimation. J. Am. Stat. Assoc. 102, 359–378.

Jung, Y., 2018. Multiple predicting K-fold cross-validation for model selection. J. Nonparametr. Stat. 30, 197–215.

Khedr, M.Z., Al Desouky, A.A., Kamh, S., Hauzenberger, C., Arai, S., Tamura, A., Whattam, S.A., Morishita, T., Lasheen, E.S.R., El-Awady, A., 2023. Petrogenesis of Gerf Neoproterozoic carbonatized peridotites (Egypt): Evidence of convergent margin metasomatism of depleted sub-arc mantle. Lithos 450–451, 107192. https://doi.org/10.1016/J.LITHOS.2023.107192.

Kokhanovsky, A., Di Mauro, B., Colombo, R., 2022. Snow surface properties derived from PRISMA satellite data over the Nansen Ice Shelf (East Antarctica). Front. Environ. Sci. 10, 1420. https://doi.org/10.3389/FENVS.2022.904585/BIBTEX.

Le Rest, K., Pinaud, D., Monestiez, P., Chadoeuf, J., Bretagnolle, V., 2014. Spatial leave-one-out cross-validation for variable selection in the presence of spatial autocorrelation. Glob. Ecol. Biogeogr. 23, 811–820.

Loizzo, R., Daraio, M., Guarini, R., Longo, F., Lorusso, R., DIni, L., Lopinto, E.,, 2019. Prisma Mission Status and Perspective. Int. Geosci. Remote Sens. Symp. 4503–4506 https://doi.org/10.1109/IGARSS.2019.8899272.

Macusi, E.D., Estor, D.E.P., Borazon, E.Q., Clapano, M.B., Santos, M.D., 2022. Environmental and Socioeconomic Impacts of Shrimp Farming in the Philippines: A Critical Analysis Using PRISMA. Sustain. 2022, Vol. 14, Page 2977 14, 2977. https://doi.org/10.3390/SU14052977.

Marcot, B.G., Hanea, A.M., 2021. What is an optimal value of k in k-fold cross-validation in discrete Bayesian network analysis? Comput. Stat. 36, 2009–2031. https://doi.org/10.1007/s00180-020-00999-9.

Meyer, H., Reudenbach, C., Hengl, T., Katurji, M., Nauss, T., 2018. Improving performance of spatio-temporal machine learning models using forward feature selection and target-oriented validation. Environ. Model. Softw. 101, 1–9.

Nadi, A., Moradi, H., 2019. Increasing the views and reducing the depth in random forest. Expert Syst. Appl. 138, 112801 https://doi.org/10.1016/j.eswa.2019.07.018.

Niroumand-Jadidi, M., Bovolo, F., Bresciani, M., Gege, P., Giardino, C., 2022. Water Quality Retrieval from Landsat-9 (OLI-2) Imagery and Comparison to Sentinel-2. Remote Sens. 14 https://doi.org/10.3390/rs14184596.

Phinzi, K., Abriha, D., Szabó, S., 2021. Classification Efficacy Using K-Fold Cross-Validation and Bootstrapping Resampling Techniques on the Example of Mapping Complex Gully Systems. Remote Sens. 13 https://doi.org/10.3390/rs13152980.

Pohjankukka, J., Pahikkala, T., Nevalainen, P., Heikkonen, J., 2017. Estimating the prediction performance of spatial models via spatial k-fold cross validation. Int. J. Geogr. Inf. Sci. 31, 2001–2019.

Pradham, P., Younan, N.H., King, R.L., 2008. Concepts of image fusion in remote sensing applications. Academic.

Prasad, H.C., Bhalla, P., Palria, S., 2014. Site suitability analysis of water harvesting structures using remote sensing and GIS–A case study of Pisangan watershed, Ajmer District, Rajasthan. Int. Arch. Photogramm. Remote Sens. Spat. Inf. Sci. 40, 1471–1482.

Rokach, L., 2010. Ensemble-based classifiers. Artif. Intell. Rev. 33, 1–39.

Roy, D.K., Paul, C.R., Munmun, T.H., Datta, B., 2024. An automatic model selection-based machine learning approach to predict seawater intrusion into coastal aquifers. Environ. Earth Sci. 83, 287.

Shebl, A., Abdellatif, M., Hissen, M., Ibrahim Abdelaziz, M., Csámer, Á., 2021. Lithological mapping enhancement by integrating Sentinel 2 and gamma-ray data utilizing support vector machine: A case study from Egypt. Int. J. Appl. Earth Obs. Geoinf. 105, 102619 https://doi.org/10.1016/J.JAG.2021.102619.

Shebl, A., Abdelaziz, M.I., Ghazala, H., Araffa, S.A.S., Abdellatif, M., Csámer, Á., 2022. Multi-criteria ground water potentiality mapping utilizing remote sensing and geophysical data: A case study within Sinai Peninsula. Egypt. Egypt. J. Remote Sens. Sp. Sci. 25, 765–778.

Shebl, A., Abriha, D., Fahil, A.S., El-Dokouny, H.A., Elrasheed, A.A., Csámer, Á., 2023a. PRISMA hyperspectral data for lithological mapping in the Egyptian Eastern Desert: Evaluating the Support Vector Machine, Random Forest, and XG Boost Machine Learning Algorithms. Ore Geol, Rev, p. 105652.

Shebl, A., El-Desoky, H.M., Abdel-Rahman, A.M., Fahmy, W., El-Awny, H., El-Sherif, A., El-Rahmany, M.M., Csámer, Á., 2023b. Impact of DEMs for Improvement Sentinel 2 Lithological Mapping Utilizing Support Vector Machine: A Case Study of Mineralized Fe-Ti-Rich Gabbroic Rocks from the South Eastern Desert of Egypt. Minerals 13, 826.

Shebl, A., Badawi, M., Dawoud, M., Abd El-Wahed, M., El-Dokouny, H.A., Csámer, Á., 2024. Novel comprehensions of lithological and structural features gleaned via Sentinel 2 texture analysis. Ore Geol. Rev. 168, 106068 https://doi.org/10.1016/j.oregeorev.2024.106068.

Shebl, A., Csámer, Á., 2021. Stacked vector multi-source lithologic classification utilizing Machine Learning Algorithms: Data potentiality and dimensionality monitoring.

Remote Sens. Appl. Soc. Environ. 100643 https://doi.org/10.1016/J.RSASE.2021.100643.

Stern, R.J., 1994. Arc-assembly and continental collision in the Neoproterozoic African orogen: implications for the consolidation of Gondwanaland. Annu. Rev. Earth Planet. Sci. 22, 319–351.

Sun, T., Cheng, W., Abdelkareem, M., Al-Arifi, N., 2022. Mapping Prospective Areas of Water Resources and Monitoring Land Use/Land Cover Changes in an Arid Region Using Remote Sensing and GIS Techniques. Water 14. https://doi.org/10.3390/w14152435.

Wang, W., Xue, C., Zhao, J., Yuan, C., Tang, J., 2024. Machine learning-based field geological mapping: A new exploration of geological survey data acquisition strategy. Ore Geol, Rev, p. 105959.

Wulder, M.A., Roy, D.P., Radeloff, V.C., Loveland, T.R., Anderson, M.C., Johnson, D.M., Healey, S., Zhu, Z., Scambos, T.A., Pahlevan, N., et al., 2022. Fifty years of Landsat science and impacts. Remote Sens. Environ. 280, 113195.

Yadav, S., Shukla, S., 2016. Analysis of k-Fold Cross-Validation over Hold-Out Validation on Colossal Datasets for Quality Classification, in: 2016 IEEE 6th International Conference on Advanced Computing (IACC). pp. 78–83. https://doi.org/10.1109/IACC.2016.25.

Yaloveha, V., Podorozhniak, A., Kuchuk, H., 2022. Convolutional neural network hyperparameter optimization applied to land cover classification. Radioelectron. Comput. Syst. 115–128.

Yates, L.A., Richards, S.A., Brook, B.W., 2021. Parsimonious model selection using information theory: a modified selection rule. Ecology 102, e03475.

Yates, L.A., Aandahl, Z., Richards, S.A., Brook, B.W., 2023. Cross validation for model selection: a review with examples from ecology. Ecol. Monogr. 93, e1557.

Zoheir, B., El-Wahed, M.A., Pour, A.B., Abdelnasser, A., 2019. Orogenic gold in transpression and transtension zones: Field and remote sensing studies of the barramiya–mueilha sector. Egypt. Remote Sens. 11, 2122.